JCB Journal of Cell Biology

ARTICLE

TDP-43 mediates SREBF2-regulated gene expression required for oligodendrocyte myelination

Wan Yun Ho[1*], Jer-Cherng Chang[1*], Kenneth Lim[1,2*], Amaury Cazenave-Gassiot[3,4], Aivi T. Nguyen[5], Juat Chin Foo[4], Sneha Muralidharan[4], Ashley Viera-Ortiz[5], Sarah J.M. Ong[1], Jin Hui Hor[6], Ira Agrawal[1], Shawn Hoon[7], Olubankole Aladesuyi Arogundade[8], Maria J. Rodriguez[8], Su Min Lim[9,10], Seung Hyun Kim[9], John Ravits[8], Shi-Yan Ng[1,6], Markus R. Wenk[3,4], Edward B. Lee[5], Greg Tucker-Kellogg[2,11], and Shuo-Chien Ling[1,12,13]

Cholesterol metabolism operates autonomously within the central nervous system (CNS), where the majority of cholesterol resides in myelin. We demonstrate that TDP-43, the pathological signature protein for amyotrophic lateral sclerosis (ALS) and frontotemporal dementia (FTD), influences cholesterol metabolism in oligodendrocytes. TDP-43 binds directly to mRNA of SREBF2, the master transcription regulator for cholesterol metabolism, and multiple mRNAs encoding proteins responsible for cholesterol biosynthesis and uptake, including *HMGCR*, *HMGCS1*, and *LDLR*. TDP-43 depletion leads to reduced SREBF2 and LDLR expression, and cholesterol levels in vitro and in vivo. TDP-43–mediated changes in cholesterol levels can be restored by reintroducing SREBF2 or LDLR. Additionally, cholesterol supplementation rescues demyelination caused by TDP-43 deletion. Furthermore, oligodendrocytes harboring TDP-43 pathology from FTD patients show reduced HMGCR and HMGCS1, and coaggregation of LDLR and TDP-43. Collectively, our results indicate that TDP-43 plays a role in cholesterol homeostasis in oligodendrocytes, and cholesterol dysmetabolism may be implicated in TDP-43 proteinopathies–related diseases.

Introduction

Although the central nervous system (CNS) accounts for only ∼2% of body weight, 25% of total cholesterol resides in the CNS. Within the CNS, 70–80% of cholesterol resides in myelin, with the remaining 20–30% situated in the membranous organelles and plasma membranes of neurons and other glia (Dietschy and Turley, 2004). In addition to insulating the axons for saltatory conduction, myelin also provides the neurons with energy and metabolic support essential for the functional integrity of the nervous system (Nave and Werner, 2014; Lee et al., 2012). Furthermore, myelin can be regulated by neuronal activity (Wake et al., 2011; Gibson et al., 2014), and this lifelong myelin plasticity may influence learning, such as the development of new motor skills (McKenzie et al., 2014; Hill et al., 2018). Although myelin is the continuous extension of the plasma membrane, the lipid and protein composition of myelin is distinct, reflecting its specialized function (Nave and Werner, 2014). In particular, myelin has a much higher lipid content (70–75%) compared with the plasma membrane (∼30%; Dietschy and Turley, 2004). Cholesterol accounts for 25–30% of the total lipids in myelin (Dietschy and Turley, 2004), which is 10–20-fold more abundant when compared with the ER. Furthermore, the majority of cholesterol is synthesized locally within the CNS with limited import from the peripheral circulation (Jurevics and Morell, 1995; Quan et al., 2003). The myelination surface is estimated to expand as much as 5,000 μm² per day in rodents during active myelination (Pfeiffer et al., 1993), implying a high demand for cholesterol biosynthesis. It is assumed that astrocytes and oligodendrocytes are the major cell types producing cholesterol within the CNS (Saher and Stumpf, 2015). Indeed, inactivation of cholesterol biosynthesis in either oligodendrocytes or astrocytes or both is sufficient to cause hypomyelination phenotypes (Saher et al., 2005; Camargo et al., 2012, 2017). Therefore, the cholesterol

[1]Department of Physiology, Yong Loo Lin School of Medicine, National University of Singapore, Singapore; [2]Computational Biology Programme, Faculty of Science, National University of Singapore, Singapore; [3]Department of Biochemistry, Yong Loo Lin School of Medicine, National University of Singapore, Singapore; [4]Singapore Lipidomics Incubator, Life Sciences Institute, National University of Singapore, Singapore; [5]Translational Neuropathology Research Laboratory, Department of Pathology and Laboratory Medicine, University of Pennsylvania, Philadelphia, PA; [6]Institute of Molecular and Cell Biology, A*STAR Research Entities, Singapore; [7]Molecular Engineering Laboratory, A*STAR Research Entities, Singapore; [8]Department of Neurosciences, University of California, San Diego, La Jolla, CA; [9]Department of Neurology, and Biomedical Research Institute, Hanyang University College of Medicine, Seoul, South Korea; [10]Department of Neurology, Massachusetts General Hospital, Harvard Medical School, Boston, MA; [11]Department of Biological Sciences, National University of Singapore, Singapore; [12]Healthy Longevity Translational Research Programme, Yong Loo Lin School of Medicine, National University of Singapore, Singapore; [13]Program in Neuroscience and Behavior Disorders, Duke–National University of Singapore Medical School, Singapore.

*W.Y. Ho, J.-C. Chang, and K. Lim contributed equally to this paper; Correspondence to Shuo-Chien Ling: phsling@nus.edu.sg.

© 2021 Ho et al. This article is distributed under the terms of an Attribution–Noncommercial–Share Alike–No Mirror Sites license for the first six months after the publication date (see http://www.rupress.org/terms/). After six months it is available under a Creative Commons License (Attribution–Noncommercial–Share Alike 4.0 International license, as described at https://creativecommons.org/licenses/by-nc-sa/4.0/).

required for myelination comes from at least two sources: de novo synthesis within oligodendrocytes and the transfer and uptake from astrocytes.

Since cholesterol is an essential component of all membranes and animal cells cannot degrade cholesterol, multiple mechanisms are used to maintain cholesterol homeostasis. The mechanisms governing cholesterol metabolism have been elegantly illustrated by the Brown and Goldstein laboratories (Brown and Goldstein, 2009; Brown et al., 2018; Goldstein and Brown, 2015). Cholesterol is synthesized de novo from acetyl-CoA via sequential actions of at least 19 biosynthetic enzymes and imported via low-density lipoprotein receptors (LDLRs) that bind to the circulating cholesterol-containing lipoproteins. Genes encoding cholesterol biosynthesis such as 3-hydroxy-3-methylglutaryl coenzyme A (HMG-CoA) synthase (HMGCS), HMG-CoA reductase (HMGCR), and LDLRs, are modulated through the feedback control of sterol regulatory element–binding factors (SREBFs, also known as sterol regulatory element–binding proteins [SREBPs]; Horton et al., 2003; Brown et al., 2018). SREBFs are encoded by two genes, *SREBF1* and *SREBF2*, the former of which uses two alternative transcription start sites to generate SREBF1A and SREBF1C isoforms. SREBF1 and SREBF2 have been shown to regulate fatty acid and cholesterol metabolism, respectively (Horton et al., 2003, 2002). Full-length SREBF1s and SREBF2s reside in the ER by binding to SREBF cleavage activation protein (SCAP), which in turn binds to insulin-induced gene 1/2 (INSIG1/2). When intracellular sterol concentration is low, INSIG1/2 dissociates from SCAP, allowing SREBFs and SCAP to translocate into the Golgi. Subsequently, SREBFs are sequentially cleaved by two proteolytic enzymes, site-1 and -2 proteases (S1P and S2P), encoded by *MBTPS1* and *MBTPS2*, respectively. This cleavage releases the basic-helix-loop-helix-leucine zipper (bHLH) transcription factor domain into the nucleus to activate transcription of genes involved in cholesterol biosynthesis and import (Brown et al., 2018). This SREBF-mediated feedback mechanism has also been speculated to operate within the CNS (Engelking et al., 2018).

Given cholesterol's essential role in animal physiology, genetic mutations within cholesterol metabolism pathways have been associated with at least 12 inherited diseases (Platt et al., 2014; Björkhem et al., 2010). Since cholesterol is a major component of myelin, some of these diseases are invariably accompanied by hypomyelination phenotypes (Saher and Stumpf, 2015). For example, patients with Smith–Lemli–Optiz syndrome, which is caused by mutations in the *DHCR7* gene that converts 7-dehydrocholesterol to cholesterol, exhibit agenesis (failed development) or hypoplasia (underdevelopment) of corpus callosum (Ryan et al., 1998). Furthermore, cholesterol dyshomeostasis is associated with most neurodegenerative diseases (Martín et al., 2014), including Alzheimer's disease (AD), Parkinson's disease, Huntington's disease, and amyotrophic lateral sclerosis (ALS). Although dysregulated cholesterol levels in both serum and cerebrospinal fluid have been implicated in ALS (Mariosa et al., 2017; Zeng and Zhou, 2019; Bandres Ciga et al., 2019), the mechanisms underlying cholesterol dysmetabolism in ALS remain elusive.

TDP-43 aggregations are the defining pathological hallmark found in most ALS patients and ∼45% of frontotemporal dementia (FTD) patients (Neumann et al., 2006; Ling et al., 2013; Tan et al., 2017). These "TDP-43 proteinopathies" are also observed in other adult-onset neurodegenerative diseases (Lagier-Tourenne et al., 2010), including AD (Josephs et al., 2014) and hippocampal sclerosis (Aoki et al., 2015). These suggest that TDP-43 is crucial for maintaining CNS health. TDP-43 pathology is characterized by nuclear or cytoplasmic aggregation with loss of normal nuclear TDP-43 in neurons and glia. This indicates that both loss of TDP-43 functions and gain of toxic properties in neurons and glia may contribute to TDP-43–mediated diseases (Lee et al., 2011; Ling et al., 2013). Furthermore, abundant oligodendroglial TDP-43 inclusions are associated with an aggressive subtype of FTD (Lee et al., 2017), suggesting potential TDP-43 dysfunctions within oligodendrocytes. We have previously shown that TDP-43 is cell-autonomously required for survival and myelination in mature oligodendrocytes (Wang et al., 2018). Specifically, oligodendroglial TDP-43 deletion down-regulates myelin-related genes and triggers necroptosis in mature oligodendrocytes, both of which contribute to the demyelination phenotype (Wang et al., 2018). Here, we showed that there is a progressive and pathway-wide disruption on SREBF2-mediated cholesterol metabolism caused by oligodendroglial TDP-43 deletion. Molecularly, TDP-43 binds directly to mRNA encoding SREBF2 as well as to multiple mRNAs encoding proteins involved in cholesterol biosynthesis and uptake, including *HMGCR*, *HMGCS1*, and *LDLR*. Depletion of TDP-43 leads to reduced SREBF2 and cholesterol levels in vitro and in vivo. Furthermore, TDP-43 regulates SREBF2 and LDLR expression via transcription and translation-based mechanisms. The cholesterol reduction can be rescued by reintroducing either the nuclear portion of SREBF2 or LDLR. Supplementation of cholesterol rescues the demyelination phenotype in TDP-43 deleted oligodendrocytes. Reduced HMGCR and HMGCS1 as well as coaggregation of LDLR and TDP-43 were observed in TDP-43 pathology–bearing oligodendrocytes from FTD patients. Taken together, our data demonstrate that TDP-43 is essential for oligodendrocyte myelination by regulating SREBF2-mediated cholesterol metabolism.

Results

Distinct gene expression changes due to TDP-43 deletion in oligodendrocytes

We have previously shown that TDP-43 is cell-autonomously required for survival and myelination in mature oligodendrocytes (Wang et al., 2018). Specifically, oligodendroglial TDP-43 deletion mice developed progressive neurological phenotypes leading to early lethality. These phenotypes were accompanied by necroptotic death of mature oligodendrocytes and progressive demyelination. Although oligodendrocyte precursor cells (OPCs) in the white matter increased proliferation to compensate the loss of oligodendrocytes, gray matter OPCs showed an age-dependent decline in regeneration capacity (summarized in Fig. 1 A; Wang et al., 2018). To investigate the underlying molecular mechanisms of oligodendroglial dysfunctions and demyelination induced by TDP-43 deletion, we performed RNA sequencing (RNA-seq) on the spinal cord RNA from postnatal

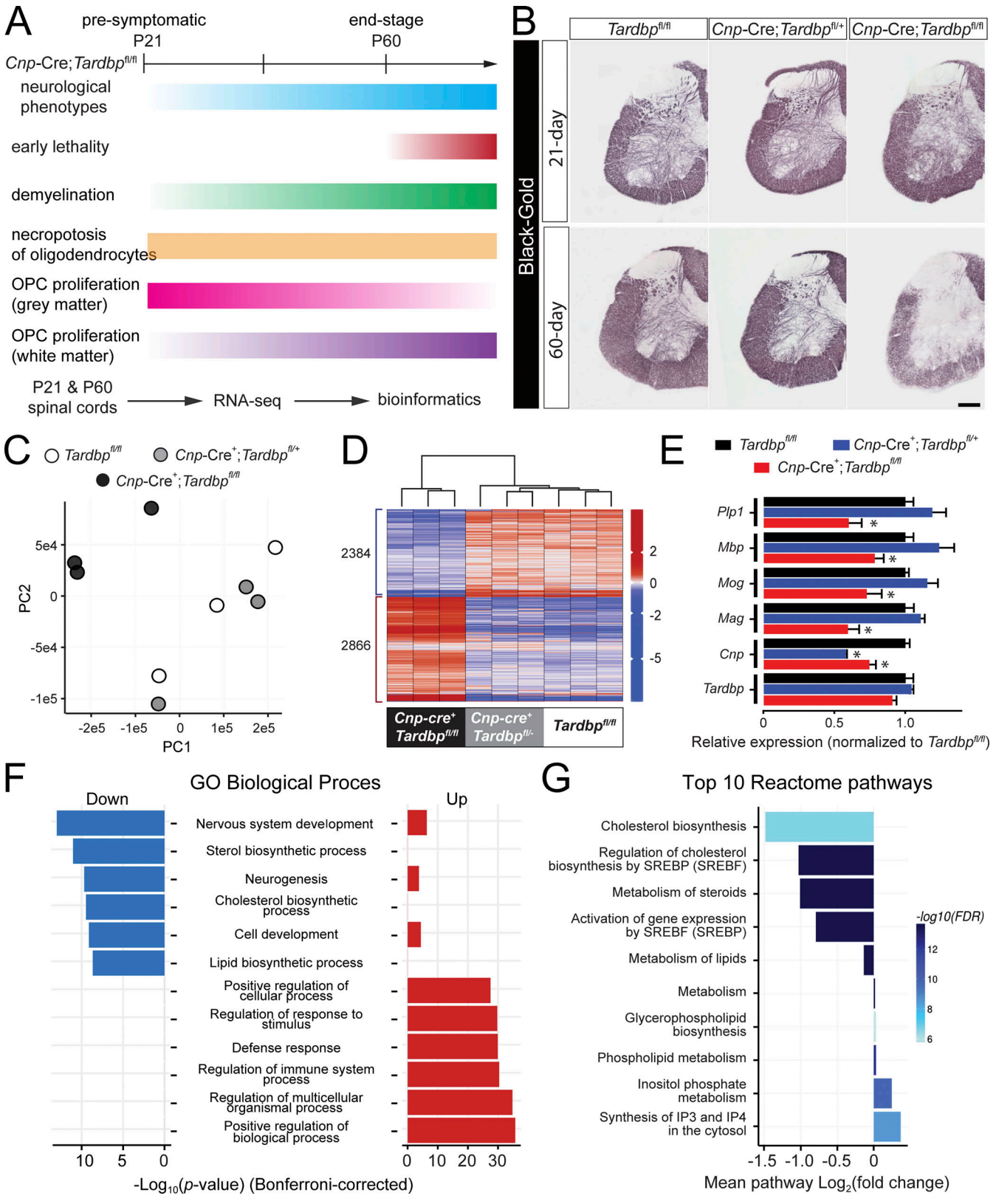

Figure 1. **Distinct expression profiles in mice with oligodendroglial TDP-43 deletion. (A)** Graphic summary of phenotypes and symptoms of oligodendroglial TDP-43 deletion mice. Oligodendroglial TDP-43 mice showed progressive demyelination phenotypes. Spinal cords from P21 and P60 mice were used for RNA-seq analysis. **(B)** Black-Gold staining of myelin tracks in the lumbar spinal cords of *Tardbp*$^{fl/fl}$, *Cnp*-Cre;*Tardbp*$^{fl/+}$, and *Cnp*-Cre^{+};*Tardbp*$^{fl/fl}$ mice. RNAs from the whole spinal cords of *Tardbp*$^{fl/fl}$, *Cnp*-Cre;*Tardbp*$^{fl/+}$, and *Cnp*-Cre^{+};*Tardbp*$^{fl/fl}$ mice from P21 and P60 time points were subjected to RNA-seq analyses. n = 4 per genotypes for P21, n = 3 per genotypes for P60. **(C)** PCA of count data across all three conditions shows a clear separation of *Cnp*-Cre^{+}; *Tardbp*$^{fl/fl}$ samples from *Tardbp*$^{fl/fl}$ and *Cnp*-Cre;*Tardbp*$^{fl/+}$ samples across the first two principal components. **(D)** Hierarchical clustering of gene-centered count

data cleanly categorizes the data, clustering *Cnp*-Cre^{+};*Tardbp*$^{fl/fl}$ samples separately from both *Tardbp*$^{fl/fl}$ and *Cnp*-Cre;*Tardbp*$^{fl/+}$ samples. **(E)** Normalized expression information for myelin-related and knockout-related genes from P60 mice. Error bars describe expression SD, and Wald testing was done for significance. *, FDR-corrected P < 0.05. **(F)** Top six GO terms (Biological Process) for down-regulated and up-regulated genes show a clear split in function. A two-sided hypergeometric test was performed for significance, and the -log10(Bonferroni-corrected P values) are presented. **(G)** Reactome pathway projection of a selected GO term cluster reveals a marked dysregulation of cholesterol biosynthetic pathways. Statistical significance of the enrichment was tested using a two-sided hypergeometric test, and -log10(FDR-corrected P values) are reported along with mean log2(fold change) of genes in the pathways.

day (P) 21 and P60 *Tardbp*$^{fl/fl}$, *Cnp*-Cre;*Tardbp*$^{fl/+}$, and *Cnp*-Cre;*Tardbp*$^{fl/fl}$ mice. The progressive loss of myelin across the whole spinal cords in *Cnp*-Cre;*Tardbp*$^{fl/fl}$ mice was evident between P21 (presymptomatic, no overt phenotype) and P60 (end stage, demyelination, before the premature death; Fig. 1 B). Consistent with our previous study (Wang et al., 2018), pairwise comparison revealed that the global gene expression patterns in *Cnp*-Cre;*Tardbp*$^{fl/fl}$ mice were distinct from *Tardbp*$^{fl/fl}$ and *Cnp*-Cre;*Tardbp*$^{fl/+}$ mice at both time points (Fig. 1, C–E; and Fig. S1). Compared with *Tardbp*$^{fl/fl}$ mice, we observed a total of 5,250 differentially expressed genes (2,721 up-regulated genes and 2,529 down-regulated genes; false discovery rate [FDR] <0.1) at the 60-d time point in *Cnp*-Cre;*Tardbp*$^{fl/fl}$ mice (Fig. 1 D). Conversely, *Cnp*-Cre;*Tardbp*$^{fl/+}$ mice were nearly indistinguishable from *Tardbp*$^{fl/fl}$ controls with only 20 differentially expressed genes (Fig. S1, A–C). Principal component analysis (PCA; Fig. 1 C) and hierarchical clustering (Fig. 1 D) of the dataset were in line with these results. Both *Tardbp*$^{fl/fl}$ and *Cnp*-Cre;*Tardbp*$^{fl/+}$ mice were clearly separated from *Cnp*-Cre;*Tardbp*$^{fl/fl}$ mice along with the two primary principal components (Fig. 1 C). Hierarchical clustering of differentially expressed genes produced a similar result, with *Cnp*-Cre;*Tardbp*$^{fl/fl}$ samples grouped separately from *Tardbp*$^{fl/fl}$ and *Cnp*-Cre;*Tardbp*$^{fl/+}$ samples (Fig. 1 D). Consistent with the demyelination phenotype (Wang et al., 2018), mRNA expression levels for most myelin-associated proteins (*Plp1*, *Mbp*, *Mog*, and *Mag*) are reduced with no apparent change in TDP-43 expression (Fig. 1 E).

Expression profiles from P21 strongly resemble those from P60. The MA (M, mean log ratio; A, mean average) plots showed similarities between *Tardbp*$^{fl/fl}$ and *Cnp*-Cre;*Tardbp*$^{fl/+}$, with a clear difference between *Cnp*-Cre;*Tardbp*$^{fl/fl}$ and *Tardbp*$^{fl/fl}$/*Cnp*-Cre;*Tardbp*$^{fl/+}$ samples (Fig. S1, D–F). Both PCA and hierarchical clustering separated the expression profiles of *Cnp*-Cre;*Tardbp*$^{fl/fl}$ mice from *Tardbp*$^{fl/fl}$ and *Cnp*-Cre;*Tardbp*$^{fl/+}$ mice (Fig. S1, G and H). Furthermore, while the overall expression pattern was similar, we note that the fold changes of differentially expressed genes were generally smaller compared with those of 60-d time point. Therefore, changes in expression profiles are consistent with the progressive phenotypes in these animals (Fig. 1 A; Wang et al., 2018).

Initial gene ontology (GO) enrichment and network analysis of the top 400 differentially expressed genes at P60 produced a large ontological network with 309 unique nodes. Manual inspection of the network revealed several notable GO term clusters centered on sterol metabolic process, glial cell development, and inflammatory response. Further enrichment of down-regulated and up-regulated genes revealed a clear functional divergence between down-regulated and up-regulated gene sets (Fig. 1 F). Among the top six down-regulated GO terms, three were associated with lipid metabolism (sterol biosynthetic process, cholesterol biosynthetic process, and lipid biosynthetic process) and two with neurogenesis and neuronal development. In contrast, up-regulated terms minimally overlapped with down-regulated terms, with the top six associated with the general biological properties (positive regulation of biological/cellular processes and organismal regulation), and three immune response–related terms (regulation of immune response and response regulation to stimulus defense; Fig. 1 F).

A progressive and pathway-wide disruption of cholesterol biosynthesis and uptake in mice with oligodendroglial TDP-43 deletion

Since lipid and sterol metabolism was over-represented in the down-regulated gene dataset, we mapped all differentially expressed genes bounded by cluster GO terms to the Reactome database along with their respective expression changes. Analysis of the Reactome networks bounded by the cluster gene set revealed a number of dysregulated pathways centering on cholesterol biosynthesis, sterol biosynthesis, and SREBF regulation–related pathways (Fig. 1 G). Srebf2 is the master regulator for cholesterol metabolism and is processed post-translationally to release its transcription factor domain (Horton et al., 2002). Thus, we examined whether Srebf2 processing machinery was affected (Fig. 2 A). Of these, only *Srebf2* and *Insig1* showed a progressive reduction in *Cnp*-Cre;*Tardbp*$^{fl/fl}$ mice between P21 and P60, whereas *Scap*, *Mbtps1*, *Mbtps2*, and *Insig2* expressions remained unchanged, suggesting that the regulated proteolytic regulation of SREBF2 is intact (Fig. 2 B). In contrast, *Srebf1* expression was elevated at both P21 and P60 in *Cnp*-Cre;*Tardbp*$^{fl/fl}$ mice (Fig. S2, A–C), suggesting that TDP-43 deletion in oligodendrocytes selectively targets the Srebf2 pathway.

Progressive reduction of *Srebf2*, which is the master transcription regulator for cholesterol metabolism, predicts a disruption in cholesterol metabolism. Indeed, further analysis of the cholesterol biosynthetic pathway revealed a progressive and pathway-wide repression (Fig. 2, C and D). 17 of 19 genes (*Acat2, Hmgcs1, Hmgcr, Mvk, Pmvk, Mvd, Idl1, Fdps, Fdft1, Sqle, Lss, Dhcr24, Cyp51, Nsdhl, Ebp, Sc5d,* and *Dhcr7*) involved in cholesterol biosynthesis were progressively and significantly down-regulated (Fig. 2, C and D). Age-dependent reduction in *Srebf2*, *Hmgcs1*, *Hmgcr*, *Fdft1*, and *Sqle* was further confirmed by reverse transcription quantitative polymerase chain reaction (RT-qPCR; Fig. S2 D). Since cholesterol is a key component for myelin, the progressive myelin deficits in the spinal cords of *Cnp*-Cre;*Tardbp*$^{fl/fl}$ mice (Fig. 1 B; see also Wang et al., 2018) are likely due, at least in part, to down-regulated Srebf2 and its downstream targets on cholesterol biosynthesis.

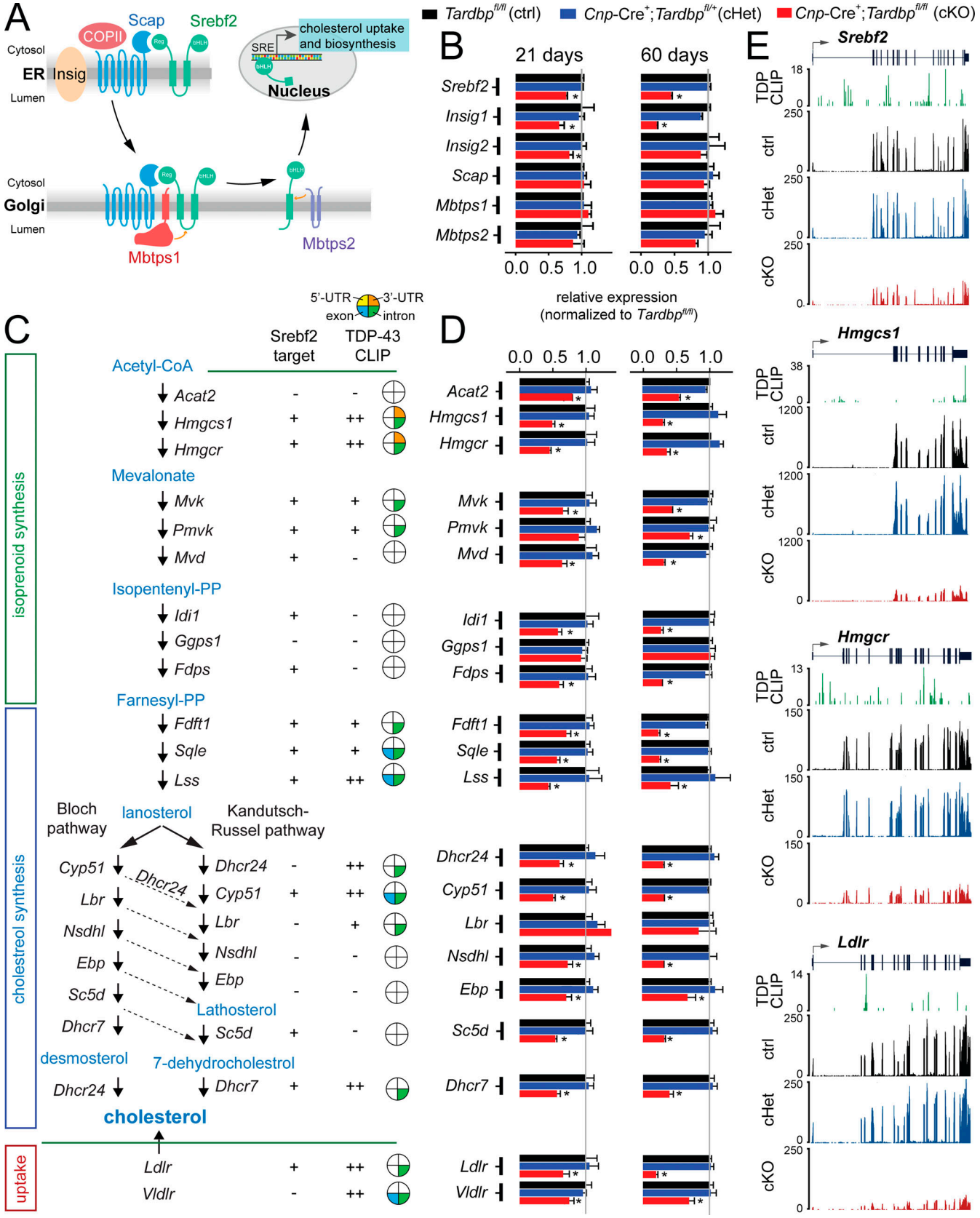

Figure 2. **Progressive and pathway-wide disruption of cholesterol metabolism in mice with oligodendroglial TDP-43 deletion. (A)** Overview of SREBF2 regulation on cholesterol biosynthesis and uptake (adapted from Brown et al., 2018). **(B)** Normalized gene expression data for Srebf2 and Srebf2-processing related genes. *, FDR-corrected P value <0.1 for *Cnp*-Cre+;*Tardbp*fl/fl versus *Cnp*-Cre+;*Tardbp*fl/+contrast. Error bars describe expression SD, and

significance was tested using the Wald test. Black bar: *Tardbp*$^{fl/fl}$ (control, ctrl); blue bar: *Cnp*-Cre;*Tardbp*$^{fl/+}$ (conditional heterozygous knockout, cHet), and red bar: *Cnp*-Cre^{+};*Tardbp*$^{fl/fl}$ (conditional knockout, cKO). n = 4 per genotypes for P21, n = 3 per genotypes for P60. **(C)** Overview of the cholesterol biosynthetic and uptake pathway. Srebf2 target track represents genes annotated as regulated by SREBF2. CLIP-seq track represents genes with CLIP-seq TDP-43 binding sites and location by combining our previous data and the public CLIP-seq assembly. +: Moderate confidence; two or more peaks on previous data or presence in two or more public datasets. ++: High confidence; more than six peaks on previous data or presence in four or more public datasets. Binding site location on gene in intronic region, exons, 5′-UTR, and 3′-UTR are colored green, blue, yellow, and orange, respectively. **(D)** Gene expression data of TDP-43 double-knockout samples reveal a near global down-regulation of cholesterol pathway–related genes. The phenotype was observed to progressively worse, with larger reductions in 60-d-old mice when compared with 21 d of age. *, FDR-corrected P value <0.1 for *Cnp*-Cre;*Tardbp*$^{fl/fl}$ versus *Cnp*-Cre;*Tardbp*$^{fl/+}$ contrast. Error bars describe expression SD, and significance was tested using the Wald test. n = 4 per genotypes for P21, n = 3 per genotypes for P60. **(E)** Gene data summary for selected cholesterol-related genes containing gene structure model, CLIP-seq coverage (green), and RNA-seq coverage for *Tardbp*$^{fl/fl}$ (black, ctrl), *Cnp*-Cre;*Tardbp*$^{fl/+}$ (blue, cHet), and *Cnp*-Cre;*Tardbp*$^{fl/fl}$ (red, cKO) conditions.

In addition to de novo cholesterol biosynthesis within oligodendrocytes, the "horizontal cholesterol transfer" from astrocytes has been proposed to supplement cholesterol to oligodendrocytes (Saher et al., 2005). Because of progressive myelin loss and the subsequent fatal phenotype observed in the *Cnp*-Cre;*Tardbp*$^{fl/fl}$ mice, we reasoned that the horizontal cholesterol transfer pathway might also be blocked such that progressive myelin loss could not recover. Both *Ldlr* and very-low-density lipoprotein receptor (*Vldlr*) are expressed in oligodendrocytes (Zhao et al., 2007). Thus, they are likely candidates for cholesterol uptake. RNA-seq data reveal a progressive reduction of *Ldlr* and *Vldlr*, with the former reduced to 20% by 60 d of age in the *Cnp*-Cre;*Tardbp*$^{fl/fl}$ mice (Fig. 2 C). Age-dependent reduction in *Ldlr* was further confirmed by RT-qPCR (Fig. S2 D). This supports the hypothesis that both cholesterol biosynthesis and uptake are disrupted in the oligodendrocytes of *Cnp*-Cre;*Tardbp*$^{fl/fl}$ mice. It is worth mentioning that genes involved in cholesterol efflux, including *Apoe*, *Abcg1*, and *Abcg1*, showed an age-dependent increase between P21 and P60, suggesting a compensatory up-regulation of cholesterol efflux from the astrocytes (Fig. S2, E and F).

Reduced cholesterol metabolism and level in mice with oligodendroglial TDP-43 deletion

To investigate the reduction of SREBF2 and LDLR mRNAs in mice, we performed RNA-FISH to colabel TDP-43, SREBF2, and LDLR mRNAs (Fig. S3). Quantification of RNA-FISH signal revealed that LDLR mRNA signals was reduced across the whole spinal cord, including dorsal and ventral gray matter and white matter (Fig. S3 B), while TDP-43 and SREBF2 had reductions in ventral and dorsal gray matter, but not white matter, of oligodendroglial TDP-43 deletion mice (Fig. S3, C and D). The failure to detect the reduction of SREBF2 and TDP-43 FISH signals in the white matter is likely due to inability to identify the oligodendrocytes specifically as other cell types also express SREBF2 and TDP-43. To circumvent this limitation and further confirm that the reduction of SREBF2 and LDLR mRNAs is specific in TDP-43-deleted oligodendrocytes, we combined RNA fluorescence in situ hybridization (RNA-FISH) with immunofluorescence (IF) using GSTP1 to label oligodendrocytes (Fig. 3 A). To better quantify the RNA-FISH signal, we reconstructed the 3D images of individual oligodendrocytes and quantified FISH signals for TDP-43, LDLR, and SREBF2 (right, Fig. 3 A; and Video 1). Consistent with the previous IF results (Wang et al., 2018), TDP-43 mRNA is depleted in oligodendrocytes (Fig. S3, E and F). Quantification of RNA-FISH signal at P21 and P60 revealed a progressive reduction of SREBF2 (P21, 35% decrease, $P < 0.05$; P60, 65% decrease, $P < 0.01$) and LDLR (P21, 43% decrease, $P < 0.001$; P60, 95% decrease, $P < 0.001$) mRNA signals in oligodendrocytes (Fig. 3 B).

To further investigate whether there was reduced protein expression within the cholesterol metabolism pathway in oligodendrocytes, we colabeled SREBF2, HMGCS1, and LDLR with the mature oligodendrocyte marker CC1 (Bin et al., 2016). The specificities of these antibodies were confirmed by siRNA-mediated knockdown and overexpression of cDNA constructs (Fig. S4). The SREBF2, HMGCS1, and LDLR proteins were decreased in the mature oligodendrocytes across gray and white matter of *Cnp*-Cre;*Tardbp*$^{fl/fl}$ mice, but not in *Tardbp*$^{fl/fl}$ mice, at P60 (Fig. 3 E). Consistent with RNA-seq and RNA-FISH results, these protein changes were more pronounced in P60 when compared with P21.

It is worth noting that although the immunoreactivities of SREBF2 and LDLR appear to be reduced in the CC1-positive oligodendrocytes, the immunoreactivities of surrounding cells appear to be increased (Fig. 3 E, left [SREBF2] and right [LDLR]). This suggests that a potential compensatory mechanism from other cell types and/or additional post-translational mechanisms of SREBF2 and LDLR processing may be dysregulated at 60 d of age. To address the first possibility, we investigated the status of astrocytes and microglia using GFAP and Iba1, respectively. Pronounced GFAP and Iba1 immunoreactivities suggest an activation of astrocytes and microglia, i.e., astrogliosis and microgliosis (Fig. 4 A; see also Peng et al., 2020). Colabeling of GFAP with LDLR (Fig. 4 B) as well as SOX9 with SREBF2 (Fig. 4 C) revealed overlapping signals, suggesting that LDLR and SREBF2 proteins are up-regulated in astrocytes. By contrast, increased SREBF2 staining did not colocalize with CD45-positive microglia (Fig. 4 D).

Given the overall reduced expression of SREBF2 and its down-stream targets, we next sought to determine the extent of cholesterol reduction in *Cnp*-Cre;*Tardbp*$^{fl/fl}$ mice. To do so, we measured the cholesterol content in the spinal cords using gas chromatography–mass spectrometry (GC/MS) at both 21- and 60-d time points. Cholesterol levels in *Cnp*-Cre;*Tardbp*$^{fl/fl}$ mice were initially comparable with those of *Tardbp*$^{fl/fl}$ and *Cnp*-Cre;*Tardbp*$^{fl/+}$ mice at P21. At P60, the cholesterol level was reduced to 60% ($P < 0.001$) of that in *Tardbp*$^{fl/fl}$, with no significant differences between *Tardbp*$^{fl/fl}$ and *Cnp*-Cre;*Tardbp*$^{fl/+}$ mice (Fig. 4 E). By contrast, phosphatidylcholine (PC) levels were similar between *Tardbp*$^{fl/fl}$ and *Cnp*-Cre;*Tardbp*$^{fl/fl}$ mice at

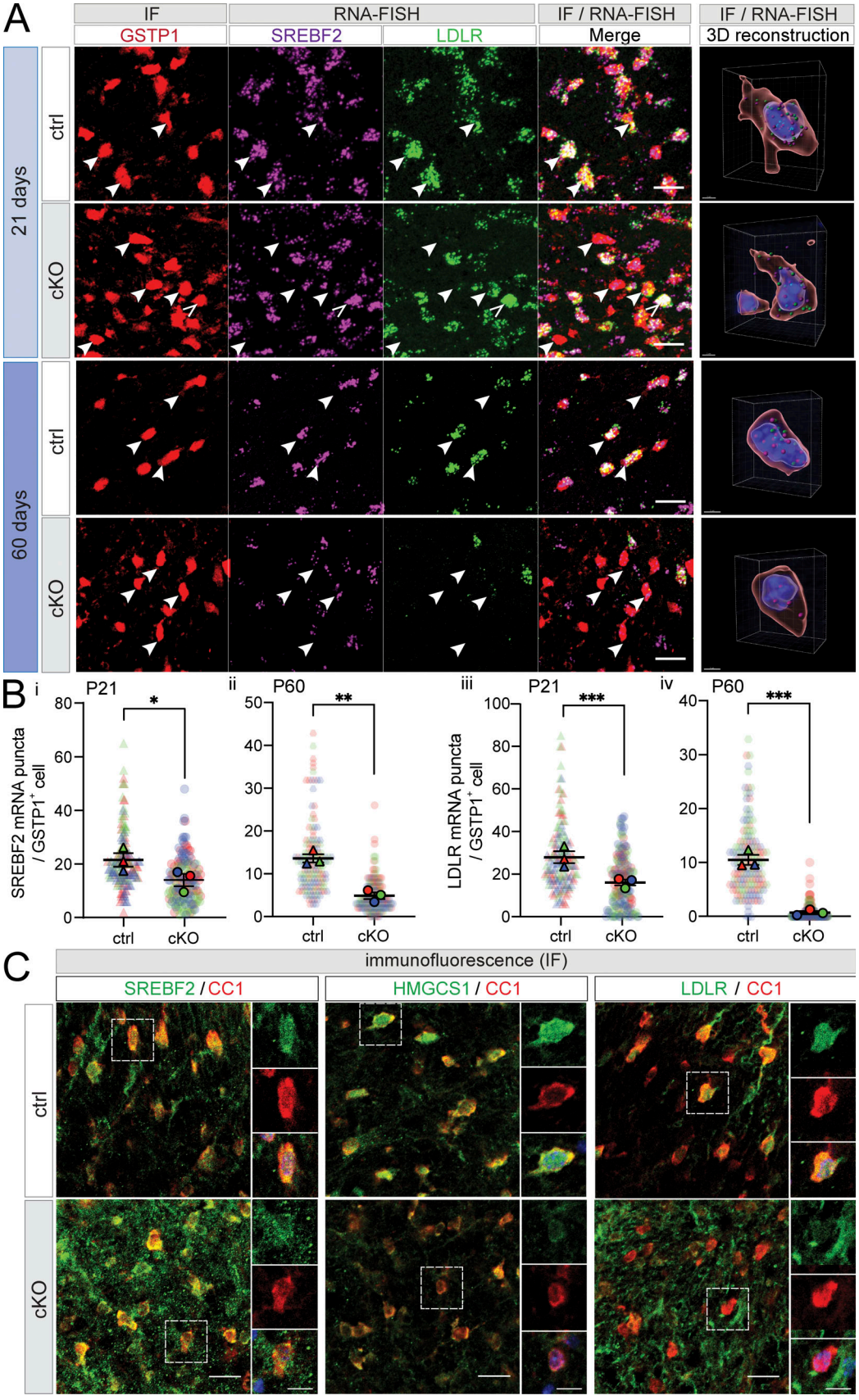

Figure 3. **Reduced SREBF2 and its downstream targets in the TDP-43–deleted oligodendrocytes. (A)** LDLR and SREBF2 mRNA expression in oligodendrocytes of ctrl and cKO mouse lumbar spinal cord (arrowhead), revealed through combined RNA fluorescent in situ hybridization (RNA-FISH) and GST-P1

IF staining. Images were taken from the ventral gray matter at P21 and P60, at 20× magnification. Scale bar: 20 µm. 3D reconstruction of oligodendrocytes for LDLR (green) and SREBF2 (magenta) mRNA quantification. DAPI (blue). Scale bar: 3 µm. **(B)** Quantification of SREBF2 (i, ii) and LDLR (iii, iv) puncta in oligodendrocytes of ctrl and cKO mouse lumbar spinal cord, at P21 (i, iii) and P60 (ii, iv). Puncta counts for individual oligodendrocytes (faded circle and triangles), and means (solid circle and triangle) for each animal (n = 3) plotted, total mean ± SEM derived from all animals. Significance was tested using unpaired t test; *, P < 0.05; **, P < 0.01; ***, P < 0.001. n = 3 per genotype, 10 cells were quantified per section, and at least five sections were quantified per animal. **(C)** Confocal images of colabeling of oligodendrocytes (CC1+, red) and key proteins involved in cholesterol metabolism (SREBF2, left; HMGCS1, middle; and LDLR, right, green) in the white matter of spinal cord sections from 60-d-old mice. Square areas were separated into individual channels, indicating reduction of SREBF2, HMGCS1, and LDLR protein in oligodendrocytes. n = 3 per genotype, six to eight slices per animals were stained and observed. Scale bar: 10 µm. Enlarged images of single cell split into individual channels for SREBF2/HMGCS1/LDLR (green) and CC1 (red). Scale bar: 10 µm. cKO, conditional knockout; ctrl, control.

both 21- and 60-d time points (Fig. 4 F). Taken together, the data indicate a selective disruption in SREBF2-mediated cholesterol metabolism under oligodendroglial TDP-43 deletion.

To independently and further verify whether SREBF2 and LDLR expression was down-regulated in mature oligodendrocytes deleted with TDP-43, primary OPCs were isolated from the spinal cords of *Tardbp*$^{fl/fl}$ and *Cnp*-Cre;*Tardbp*$^{fl/fl}$ mice. These OPCs were subsequently differentiated into oligodendrocytes for analyses (Fig. 5 A). Loss of TDP-43 was observed in myelin basic protein (MBP)–positive mature oligodendrocytes, but not in OPCs, confirming the timing of CNP (2',3'-cyclic-nucleotide 3'-phosphodiesterase)-Cre–mediated TDP-43 inactivation in mature oligodendrocytes (Fig. 5, E and G, arrowhead; see also Wang et al., 2018). RNA-FISH was used to evaluate the levels of SREBF2 and LDLR mRNAs in TDP-43–deleted oligodendrocytes (Fig. 5 B). Quantification revealed a 19% (P < 0.01) and 61% (P < 0.01) reduction of SREBF2 and LDLR mRNA signals, respectively, in TDP-43–deleted oligodendrocytes (Fig. 5, C and D). Furthermore, loss of TDP-43 correlates with reduction of SREBF2 (P < 0.001) and LDLR (P < 0.05) proteins in MBP-positive mature oligodendrocytes (Fig. 5, E–H). Reduction of LDLR protein was further confirmed by immunoblots (Fig. 5 I). Taken together, the data indicate that cholesterol metabolism is disrupted in oligodendroglial TDP-43 deletion mice due to reduced SREBF2 and LDLR protein expression in mature oligodendrocytes, at least in part by reducing SREBF2 and LDLR mRNA level.

TDP-43 regulates cholesterol metabolism essential for myelination

To elucidate how TDP-43 deletion disrupts cholesterol metabolism, we first examined the RNA binding partners of TDP-43 using our previous TDP-43 cross-linked immunoprecipitation sequencing (CLIP-seq) dataset (Polymenidou et al., 2011) and other publicly available datasets (www.ncbi.nlm.nih.gov/gds). We found 11 of 19 enzymes (*Hmgcs1*, *Hmgcr*, *Mvk*, *Pmvk*, *Fdft1*, *Sqle*, *Lss*, *Dhcr24*, *Cyp51*, *Lbr*, and *Dhcr7*) involved in cholesterol biosynthesis, and both *Ldlr* and *Vldlr* (which are involved in cholesterol uptake) are bound by TDP-43 with at least one binding peak (Fig. 2, C and E). The majority of the binding sites were located in intronic regions (Fig. 2 C). TDP-43 also binds to *Srebf2* mRNA (Fig. 2 E). We next confirmed the direct binding between TDP-43 and mRNA encoding *Srebf2*, *Hmgcs1*, *Hmgcr*, and *Ldlr* mRNA with UV cross-linking immunoprecipitation and RT-PCR analysis in the human oligodendrocyte cell line MO3.13 (Fig. 6 A). TDP-43 binds to mRNAs of *SREBF2*, *HMGCS1*, *HMGCR*, and *LDLR*, but not *MVD* (Fig. 6 B). This is consistent with the CLIP-seq data and further shows conserved TDP-43–mRNA interactions between humans and mice. Furthermore, siRNA-mediated acute knockdown of TDP-43 in the MO3.13 oligodendrocyte cell line (Fig. 6 C) reduced both full-length (31% reduction, P < 0.05) and N-terminal transcriptional domain-containing SREBF2 (64% reduction, P < 0.05) and LDLR protein (22% reduction, P = 0.057) expressions (Fig. 6 D).

Although SREBF2 and HMGCR mRNA were reduced under TDP-43 knockdown conditions (Fig. S5 A), TDP-43 does not appear to alter the half-life of SREBF2, HMGCR, and LDLR mRNA (Fig. S5 B) or change the splicing pattern. As RT-qPCR measures the steady-state mRNA level, we reasoned that the transcription rate of SREBF2 and LDLR may be affected upon TDP-43 depletion. To test this, MO3.13 cells with or without TDP-43 knocked down were treated with 5,6-dichlorobenzimidazole 1-β-D-ribofuranoside (DRB), which inhibits positive transcription elongation factor b (P-TEFb). DRB treatment results in RNA polymerase II pausing at the promoter region while allowing the RNA polymerase II engaged in elongation to finish the transcription (Singh and Padgett, 2009). Upon DRB washout, RT-qPCR was performed with the primers within the exon 1 and intron 1 of *SREBF2* and *LDLR* to assess the transcription rate of *SREBF2* and *LDLR* (Fig. 6 E). Although the transcription rate of *SREBF2* mRNA was comparable between the control and TDP-43 knockdown condition in the initial 15 min, the transcription rate was reduced to 10% (P < 0.0001) and 20% (P < 0.0001) of control at 30 and 60 min after DRB washout in the TDP-43 knockdown condition (Fig. 6 E, i). Similarly, although the transcription rate of *LDLR* mRNA was comparable between control and TDP-43 knockdown conditions in the initial 15 min, the transcription rate of *LDLR* mRNA was reduced to 30% (P < 0.0001) at 30 min after DRB washout. However, the difference was not sustained at 60 min (Fig. 6 E, ii). By contrast, there was no difference for the transcription rate of *RPLP0* mRNA (Fig. 6 E, iii). The data suggest that reduced transcription of *SREBF2* caused by TDP-43 depletion may contribute to reduced SREBF2 mRNA level.

As TDP-43 has been proposed to regulate protein translation (Wang et al., 2008; Fiesel et al., 2012; Majumder et al., 2016; Nagano et al., 2020), we next examined whether the overall translation efficiency may be affected in TDP-43 knockdown condition. Puromycin, which is used to inhibit translation, is a structural mimic of tyrosyl tRNA that acts as the acceptor of the carboxyl-activated peptide to form peptidyl-puromycin, resulting in the termination of peptide chain (Nathans, 1964). Puromycin-containing peptides can be subsequently detected and quantified using anti-puromycin antibody, a method termed the surface sensing of translation (SUnSET) assay (Schmidt et al., 2009).

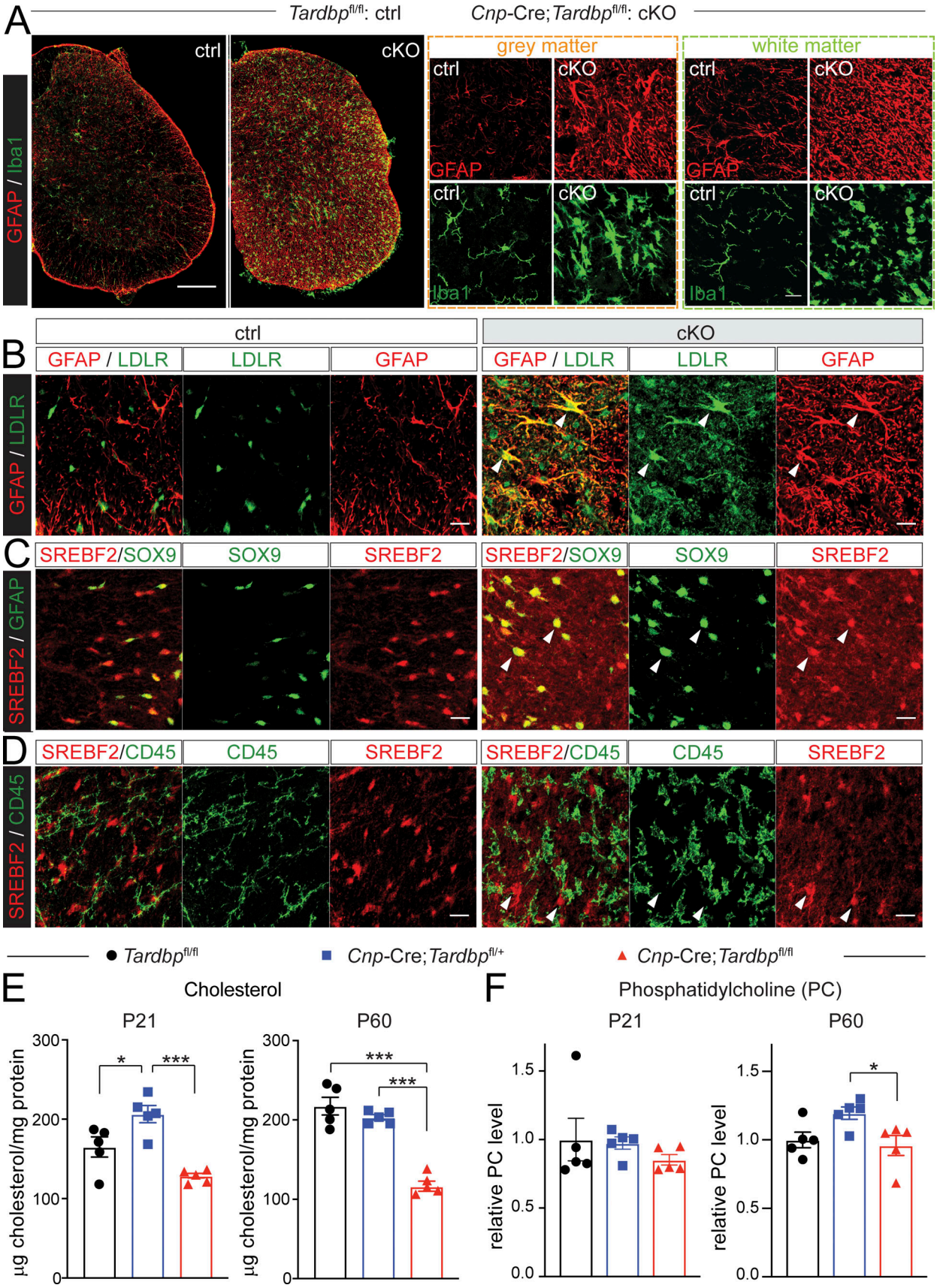

Figure 4. **Selective cholesterol reduction in the spinal cords of mice with oligodendroglial TDP-43 deletion. (A)** Confocal images of astrocytes (GFAP, red) and microglia (Iba1, green) in of spinal cord sections from *Tardbp*$^{fl/fl}$ (ctrl) and *Cnp*-Cre;*Tardbp*$^{fl/fl}$ (cKO) mice at P60. Scale bar: 200 µm. Enlarged images are

from gray matter (middle) and white matter (right). Scale bar: 20 µm. *n* = 3 per genotype, approximately six to eight slices per animals were stained and observed. **(B)** Confocal images of astrocytes (GFAP, red) with LDLR (green) in the white matter of the spinal cord sections from *Tardbp*$^{fl/fl}$ (ctrl) and *Cnp*-Cre;*Tardbp*$^{fl/fl}$ (cKO) mice at P60. Arrowhead indicates the colocalization of GFAP and LDLR signal in cKO mice. **(C)** Confocal images of astrocytes (Sox9, green) with SREBF2 (red) in the white matter of the spinal cord sections from *Tardbp*$^{fl/fl}$ (ctrl), and *Cnp*-Cre;*Tardbp*$^{fl/fl}$ (cKO) mice at P60. Arrowhead indicates the co-localization of Sox9 and SREBF2 signal in cKO mice. **(D)** Confocal images of microglia (CD45, green) with SREBF2 (red) in the white matter of the spinal cord sections from *Tardbp*$^{fl/fl}$ (ctrl) and *Cnp*-Cre;*Tardbp*$^{fl/fl}$ (cKO) mice at P60. Arrowhead indicates the SREBF2 signals without CD45 in cKO mice. **(E)** Cholesterol level was measured in *Tardbp*$^{fl/fl}$, *Cnp*-Cre;*Tardbp*$^{fl/+}$, and *Cnp*-Cre;*Tardbp*$^{fl/fl}$ spinal cord samples using GC/MS. The amount of cholesterol was normalized to protein content and expressed as micrograms cholesterol/milligrams protein. *n* = 5 per genotype per time point. One-way ANOVA with Tukey's multiple comparisons tests was used to evaluate statistical significance; *, P < 0.05; ***, P < 0.001. **(F)** PC level was measured in *Tardbp*$^{fl/fl}$, *Cnp*-Cre;*Tardbp*$^{fl/+}$, and *Cnp*-Cre;*Tardbp*$^{fl/fl}$ spinal cord samples using liquid chromatography–tandem MS. The amount of PC was normalized to protein content and compared with *Tardbp*$^{fl/fl}$. *n* = 5 per genotype per time point. One-way ANOVA with Tukey's multiple comparisons tests was used to evaluate statistical significance; *, P < 0.05. cKO, conditional knockout; ctrl, control.

We observed a 47% (P < 0.001) reduction of overall puromycin incorporation in MO3.13 cells upon TDP-43 knockdown (Fig. 6 F), indicating that global protein synthesis is impaired upon TDP-43 depletion. To further investigate whether there is a reduction in LDLR protein synthesis, puromycin-containing polypeptides were immunoprecipitated by puromycin antibody and probed with LDLR antibody. An ∼50% reduction of LDLR signal was observed upon TDP-43 knockdown (Fig. 6 F). Taken together, the data suggest that both reduced transcription rate and reduced global translation in TDP-43 knockdown condition may contribute to the reduced SREBF2 and LDLR expression.

Given the reduced SREBF2 and LDLR protein expression, we next examined the cholesterol level using filipin, a fluorescent polyene antibiotic that binds to cholesterol (Fig. 7 A). Filipin fluorescent signals were significantly reduced to ∼63% (P < 0.05) in TDP-43 and ∼56% (P < 0.05) SREBF2 knockdown cells (Fig. 7 B). Consistent with the imaging data, measurement of total cholesterol content from the cell homogenates revealed a 43% (P < 0.01) and 21% (P < 0.05) reduction of cholesterol levels in TDP-43 and SREBF2 knockdown cells, respectively (Fig. 7 C). The reduced cholesterol was further confirmed using a boradiaza-indancene (BODIPY) conjugated cholesteryl ester analogue (CholEsteryl BODIPY-FL C_{12}; 34% reduction, P < 0.05; Fig. S5 C). Since lipid droplets contain cholesterol and they regulate lipid storage, two independent dyes, BODIPY-493/503 and Nile Red, were also applied to the RNAi-treated cells. Significant reduction of BODIPY-493/503 (∼50% reduction, P < 0.05) and Nile Red (∼60% reduction, P < 0.05) fluorescence intensities were also observed in TDP-43 and SREBF2 knockdown cells (Fig. S5, D and E).

Thus far, the data suggest that TDP-43 regulates cholesterol metabolism via, at least in part, reducing the expression of SREBF2 and LDLR. To further test this hypothesis, the N-terminal transcription factor domain of SREBF2 and full-length LDLR was transiently expressed in cells with TDP-43 knockdown (Fig. 7 D). The cholesterol level can be rescued by expressing the "active" form of SREBF2 and LDLR using filipin and direct biochemical measurement for cholesterol (Fig. 7, E–G), suggesting that reduced SREBF2 and LDLR expression underlies the reduced cholesterol level observed in TDP-43 knockdown condition.

We next tested whether supplementation of cholesterol rescue the observed demyelination phenotype in TDP-43–deleted oligodendrocytes. Incubation of cholesterol-β-cyclodextrin complexes were able to rescue the MBP$^+$ area in TDP-43–deleted oligodendrocytes from 19 to 63% (P < 0.05) of the oligodendrocytes cultured from *Tardbp*$^{fl/fl}$ mice (Fig. 8, A–C). Taken together, our data indicate that TDP-43 regulates SREBF2-mediated cholesterol metabolism that is essential for myelination in oligodendrocytes. Simultaneous disruption in cholesterol biosynthesis and uptake machinery may underlie the demyelination phenotype caused by oligodendroglial TDP-43 deletion (Fig. 8 D).

Reduced cholesterol metabolism–related gene expressions in the glia from postmortem FTD patients

To further extend our findings to human settings, we colabeled TDP-43, HMGCS, and LDLR with oligodendrocyte marker (CC1) using human spinal organoid derived from induced pluripotent stem cells (iPSCs; Fig. 9 A). Results from double-labeling confirmed that TDP-43 and the cholesterol metabolism–related genes are expressed in human oligodendrocytes (Fig. 9 B).

As TDP-43 pathology is characterized by the loss of normal nuclear TDP-43 with concomitant nuclear or cytoplasmic aggregation in neurons and glia, we sought to determine whether TDP-43–dependent cholesterol deregulation can be found in cells harboring TDP-43 pathology. To this end, we examined oligodendrocytes with TDP-43 pathology in the middle frontal cortex of frontotemporal lobar degeneration with TDP-43 inclusions (FTLD-TDP) type B human brain patients (Fig. 9 C; Lee et al., 2017; Tan et al., 2017). Double staining for TDP-43/HMGCR (Fig. 9 D, top) and TDP-43/HMGCS1 (Fig. 9 D, middle) shows decreased HMGCR and HMGCS1 staining in white matter oligodendrocytes with TDP-43 inclusions (arrowheads) when compared with nonaffected glial cells (arrows). Furthermore, LDLR was colabeled with cytoplasmic TDP-43 inclusions within these white matter oligodendrocytes (Fig. 9 D, arrowheads, bottom). LDLR and TDP-43 coaggregations were not observed in glia without TDP-43 pathology (Fig. 9 D, arrow, bottom). Neither reduced HMGCR and HMGCS nor the coaggregation of LDLR and TDP-43 were observed in control samples (Fig. 9 D). The data suggests that oligodendrocytes with TDP-43 pathology have disrupted cholesterol metabolism.

Discussion

In this study, we showed that TDP-43 regulates SREBF2-mediated cholesterol metabolism essential for myelination in oligodendrocytes. Simultaneous disruptions in cholesterol

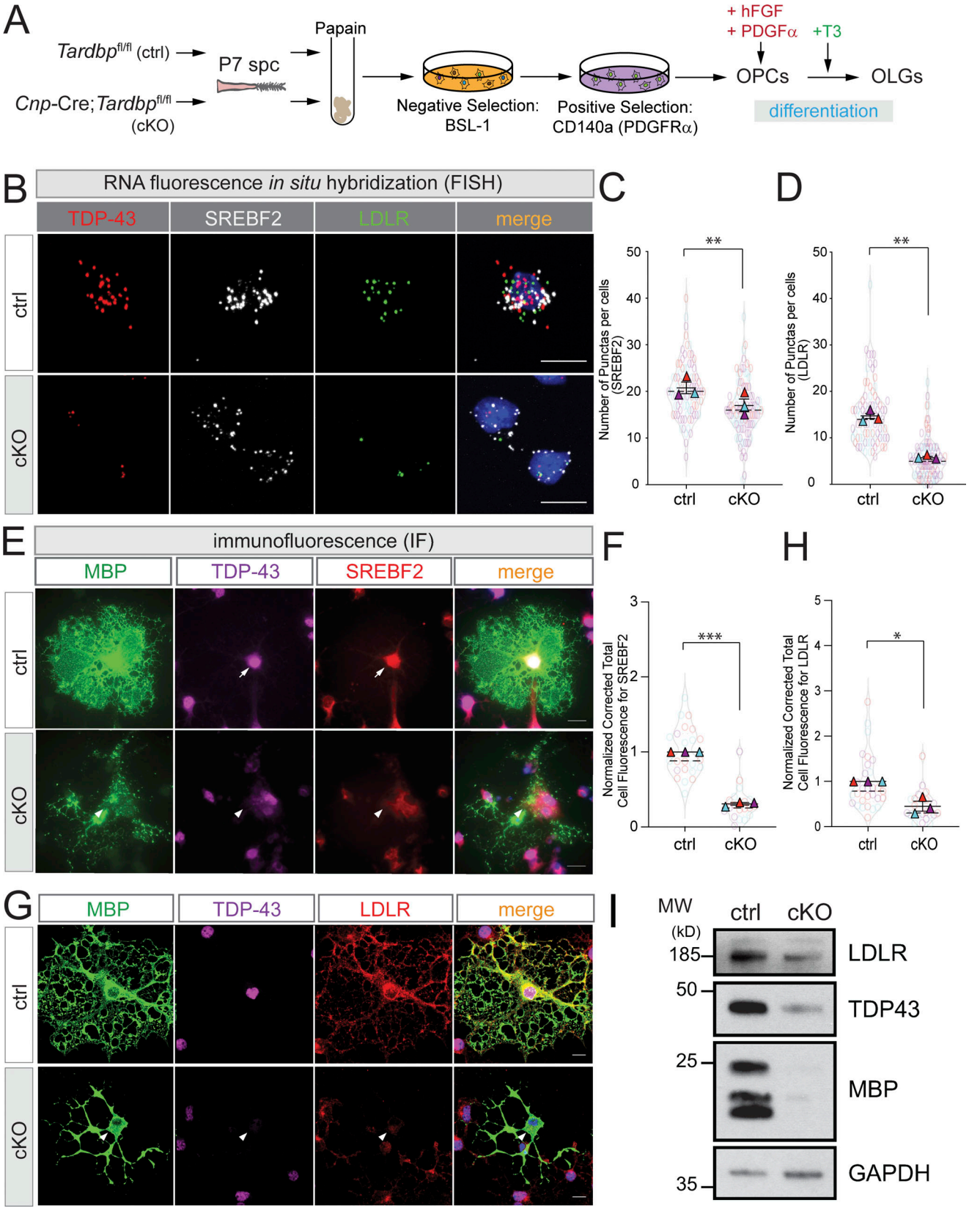

Figure 5. **TDP-43 regulates SREBF2 and LDLR expression in primary oligodendrocytes. (A)** Schematic of primary oligodendrocyte culture using immunopanning from P7 spinal cords of *Tardbp*$^{fl/fl}$ (ctrl) and *Cnp*-Cre;*Tardbp*$^{fl/fl}$ (cKO) mice. **(B)** Confocal images of RNA-FISH of SREBF2, TDP-43, and LDLR assays using primary oligodendrocyte cultured from *Tardbp*$^{fl/fl}$ (ctrl) and *Cnp*-Cre;*Tardbp*$^{fl/fl}$ (cKO) mice. **(C and D)** Quantification of FISH signals for SREBF2 (C) and LDLR (D) in ctrl and cKO oligodendrocytes. Puncta counts for individual oligodendrocytes (faded circle), and means (solid triangle) for each set of experiments

(n = 3) plotted, total mean ± SEM derived from all sets of experiments. Significance was tested using unpaired t test; **, P < 0.01. n = 3 per genotype, at least 20 cells were quantified per genotype per set of experiments. **(E–H)** Immunofluorescent staining of MBP (green; E and G), SREBF2 (red; E), LDLR (red; G), and TDP-43 (magenta; E and G) using differentiated oligodendrocytes from spinal cords of *Tardbp*$^{fl/fl}$ (ctrl) and *Cnp*-Cre;*Tardbp*$^{fl/fl}$ (cKO) mice, respectively. Oligodendrocytes without TDP-43 expression showed reduced SREBF2 (arrowhead) and LDLR (arrowhead). Scale bar = 10 µm. **(F and H)** Quantification of SREBF2 (F) and LDLR signal (H) in MBP-positive myelinating oligodendrocytes cultured from *Tardbp*$^{fl/fl}$ (ctrl) and *Cnp*-Cre;*Tardbp*$^{fl/fl}$ (cKO) mice. Corrected total cell fluorescence of individual oligodendrocytes (faded circle), and means (solid triangle) for each set of experiment (n = 3) plotted, total mean ± SEM derived from all sets of experiments. Significance was tested using unpaired t test; *, P < 0.05; ***, P < 0.001. n = 3 per genotype, at least 10 cells were quantified per genotype per set of experiment. **(I)** Immunoblots of LDLR, TDP-43, and MBP using lysates of primary oligodendrocytes cultured from *Tardbp*$^{fl/fl}$ (ctrl) and *Cnp*-Cre;*Tardbp*$^{fl/fl}$ (cKO) mice. GAPDH was used as a loading control. cKO, conditional knockout; ctrl, control; spc, spinal cord; MW, molecular weight.

biosynthesis and uptake, two molecular mechanisms required for all animal cells to maintain cholesterol homeostasis, are likely one of the causes of the demyelination phenotype observed in oligodendroglial TDP-43 deletion mice (Fig. 8 D; Wang et al., 2018). Furthermore, reduced levels of cholesterol biosynthetic enzymes and coaggregations of LDLR and TDP-43 are observed in the glia bearing pathological TDP-43 aggregates. These results suggest that TDP-43–mediated cholesterol dyshomeostasis may contribute to ALS and FTD, and more broadly, diseases characterized by TDP-43 proteinopathies.

The majority of cholesterol is synthesized de novo by astrocytes and oligodendrocytes within the CNS, and 75% of CNS cholesterol is in the myelin (Saher et al., 2005; Dietschy and Turley, 2004). Thus, it is not surprising that TDP-43–mediated disruption of cholesterol metabolism in oligodendrocytes contributes to the demyelination phenotype. Indeed, previous studies using oligodendroglial inactivation of *Fdft1,* the first enzyme committed to cholesterol biosynthesis, and *Scap*, which is required for SREBF1 and SREBF2 activation, led to a hypomyelination phenotype (Saher et al., 2005; Camargo et al., 2017). Since SREBF2 controls cholesterol metabolism, it is subjected to feedback control via regulated protein trafficking and proteolytic processing (Brown et al., 2018). INSIG1 is also regulated by SREBF2, where it increases INSIG1 level. Consequently, INSIG1 inhibits SREBF2 by retaining SREBF2 in the ER. Among the molecules involved in SREBF2 regulation, only *Insig1* showed a progressive reduction, further supporting the notion that cholesterol regulatory mechanisms are conserved in the CNS. Interestingly, selective astroglial inactivation of *Scap* also led to hypomyelination phenotype (Camargo et al., 2017). The hypomyelination phenotypes from oligodendroglial inactivation of *Fdft1* could eventually recover to ∼70% of those in control (Saher et al., 2005). This further highlights a horizontal cholesterol transfer between oligodendrocytes and astrocytes. Indeed, mice with simultaneous *Scap* inactivation in their oligodendrocytes and astrocytes have dramatic myelin reduction with <10% myelin thickness as compared with control animals (Camargo et al., 2017). In this study, we demonstrated that the TDP-43–mediated demyelination phenotype can be reversed by cholesterol supplementation, further supporting the critical role of horizontal cholesterol transfer among different glia. Furthermore, genes involved in cholesterol efflux such as *Apoe* and *Abcg1* are upregulated in *Cnp*-Cre;*Tardbp*$^{fl/fl}$ mice. This suggests that compensatory cholesterol transfer machinery from other glia is activated in *Cnp*-Cre;*Tardbp*$^{fl/fl}$ mice and there is close communication among the different glia involved in cholesterol metabolism. The notion of non–cell-autonomous and compensatory responses from the other glia is further supported by the enhanced LDLR and SREBF2 labeling in astrocytes in the oligodendroglial TDP-43 deletion mice.

SREBF2 itself and 13 transcription regulatory targets of SREBF2 involved with cholesterol biosynthesis (11) and uptake (2) are also mRNA targets of TDP-43. Notably, these targets include *HMGCS1*, *HMGCR*, and *LDLR*. Therefore, TDP-43 may regulate cholesterol metabolism via directly regulating mRNA expression of cholesterol metabolism genes. Indeed, SREBF2 and LDLR mRNA and protein expression are reduced in primary oligodendrocytes cultured from oligodendroglial TDP-43 deletion mice and in vivo. However, it does not appear that TDP-43 regulates the stabilities of mature mRNAs and/or splicing of these transcripts. Rather, TDP-43 influences the transcription rate of SREBF2, and to a lesser extent, LDLR. Furthermore, knocking down TDP-43 appears to reduce global protein translation, which, at least in part, leads to reduced LDLR translation. Thus, TDP-43 may regulate the expression of SREBF2 and LDLR via transcription and translation-based mechanisms, although the exact mechanisms still require further investigation. In addition, SREBF2 and LDLR are subjected to post-translational control to maintain their protein levels (Sharpe et al., 2014), indicating delicate and complicated regulatory mechanisms for maintaining cholesterol homeostasis. It is difficult to precisely dissect the relative contribution of TDP-43 and SREBF2 on the mRNA reductions of transcripts involved in cholesterol metabolism. Nevertheless, reintroducing the transcription factor domain of SREBF2 and LDLR rescues the cholesterol reduction phenotype caused by acute TDP-43 knockdown in vitro. Supplementation of cholesterol rescues the demyelination phenotypes in TDP-43–deleted oligodendrocytes. Collectively, these results indicate that SREBF2 and LDLR reductions are the main drivers of the cholesterol dyshomeostasis and subsequent demyelination under TDP-43 depletion conditions.

Thus far, the exact role of serum dyslipidemia in ALS pathogenesis remains controversial. Recent longitudinal studies and those that combine large patient datasets suggest that higher serum LDL level increases ALS risk (Mariosa et al., 2017; Zeng and Zhou, 2019; Bandres Ciga et al., 2019). By contrast, use of statins, cholesterol-lowering drugs that inhibits HMGCR, has been associated with an elevated occurrence of ALS-like conditions (Golomb et al., 2018). Furthermore, changes in cholesterol levels and their metabolites have been detected in the serum and cerebrospinal fluid from ALS patients (Abdel-Khalik et al., 2017). Although cholesterol regulation within the CNS operates independently from that in the circulation due to intact blood–brain barrier (BBB; Dietschy and Turley, 2004), recent

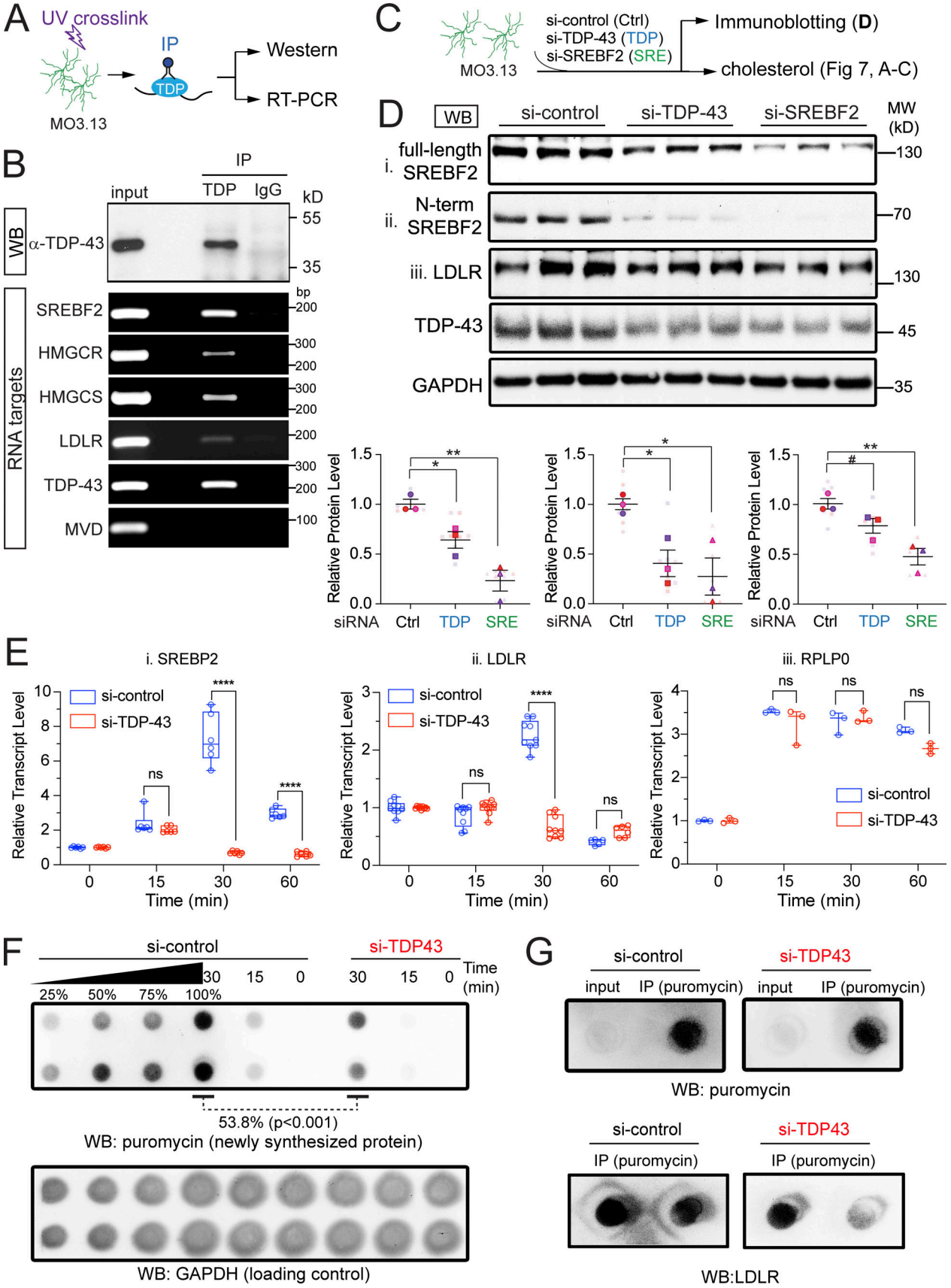

Figure 6. **TDP-43 regulates cholesterol metabolism by regulating SREBF2 and LDLR expression. (A and B)** TDP-43 binds to the *SREBF2* transcripts as well as the downstream genes controlled by SREBF2. **(A)** Schematic of CLIP. Human oligodendrocytic (M03.13) cell lysates were UV cross-linked, lysed, and

then used for TDP-43 pull-down assay. **(B)** Potential binding targets such as *SERBF2*, *HMGCR*, *HMGCS*, *LDLR*, and positive control *TARDBP* transcripts were pulled down in the TDP-43 antiserum–treated samples. **(C)** Schematic of TDP-43 and SREBF2 RNAi experiments. **(D)** Acute knockdown of TDP-43 leads to down-regulation of (i) full-length and (ii) N-terminal SREBP2 and (iii) LDLR protein levels. Human oligodendrocyte cell lines (MO3.13) were transfected with control siRNA and siRNA against TDP-43 or SREBP2. Whole-cell lysates were probed with SREBP2, LDLR, and the loading control GAPDH. Quantifications of immunoblots for (i) full-length and (ii) N-terminal SREBP2 and (iii) LDLR protein levels. Quantifications were done with three independent batch of treatments (n = 3) with three biological replicates per experiment. One-way ANOVA with Tukey's multiple comparisons tests was used to evaluate statistical significance, #, P < 0.10; *, P < 0.05; **, P < 0.01. **(E)** Newly synthesized transcripts detection by RT-qPCR in the MO3.13 cells treated with nontargeted siRNA or siRNA against TDP-43, followed by the DRB treatment. qPCR using primer pairs against the first exon-intron junction for (i) *SREBF2*, (ii) *LDLR*, and (iii) *RPLP0* detects the cDNAs from the cells collected in different intervals (0, 15, 30, and 60 min) after the removal of DRB. These gene expression levels were all normalized to no-treatment controls. Quantifications were done with three independent batch of treatments (n = 3) with three biological replicates per experiment. One-way ANOVA with Tukey's multiple comparisons tests was used to evaluate statistical significance, ****, P < 0.0001. **(F)** Global translation reduction in the MO3.13 cells with TDP-43 knockdown. The lysates from cells treated with puromycin (100 µg/ml) in 15-min intervals (0, 15, and 30 min) after the incubation non-targeted siRNA or siRNA against TDP-43 were applied onto the SUnSET assay. Quantifications were done with two independent batches of treatments with three biological replicates per experiment. One-way ANOVA with Tukey's multiple comparisons test was used to evaluate statistical significance, ****, P < 0.0001. **(G)** The MO3 cells were treated with either control or TDP-43 siRNA followed by puromycin incubation. The cells were lysed followed by immunoprecipitation with an anti-puromycin antibody, and then were blotted with LDLR antibody. Ctrl, control; N-term, N-terminal; WB, Western blot; MW, molecular weight.

studies have showed that dietary cholesterol can promote myelination in mouse models of Pelizaeus–Merzbacher disease (Saher et al., 2012) and multiple sclerosis (Berghoff et al., 2017). The therapeutic benefit may be due to BBB impairment that potentially allows the circulating cholesterol to be imported into the CNS (Berghoff et al., 2017). Indeed, BBB and blood–spinal cord barrier impairments have been reported in ALS patients and SOD1 mouse models (Winkler et al., 2013; Garbuzova-Davis et al., 2012). Thus, the role of BBB/blood–spinal cord barrier at various ALS disease states, and/or differential regulatory/compensatory mechanisms between the periphery systems and CNS, remain to be clarified. Here, we showed reduced HMGCR and HMGCS expression in TDP-43 aggregate–bearing oligodendrocytes from FTLD-TDP patients. Furthermore, LDLR appears to coaggregate with TDP-43 inclusions in the oligodendrocytes of FTLD-TDP patients. Although additional mechanisms may account for the TDP-43–LDLR coaggregation, our data indicate that TDP-43 dysfunctions, whether by loss of TDP-43 functions or formation of pathological inclusion, could cause cholesterol dyshomeostasis in the CNS.

TDP-43 may intersect with cholesterol metabolism beyond the SREBF2-mediated pathway. Recent studies suggest that *APOE4* allele increases TDP-43 pathology in hippocampal sclerosis patients (Yang et al., 2018), whereas ApoE2 allele increases FTD risk in ALS patients (Chiò et al., 2016). Furthermore, apolipoprotein E (APOE) is required to remove cholesterol crystals and subsequent remyelination during aging (Cantuti-Castelvetri et al., 2018). Our interpretation for *Apoe* up-regulation in the *Cnp*-Cre;*Tardbp*$^{f/f}$ mice is likely a compensatory mechanism for the cells to transfer more cholesterol to oligodendrocytes, rather than a direct action of TDP-43 onto APOE. Nevertheless, how ApoE may intersect with TDP-43 to regulate cholesterol metabolism and how this cross-talk may affect neuron and glia functions remain to be investigated. Recent work showed that modulation of cholesterol metabolism by small molecules can ameliorate Tau pathology in the iPSC-based AD model (van der Kant et al., 2019). Since cholesterol metabolism dysregulation may be involved in ALS, FTD, and TDP-43 proteinopathies-related disease, a similar strategy may be adapted for TDP-43–mediated disease models for potential therapeutic interventions.

Materials and methods

Mouse models

All studies were performed under protocols approved by the Institutional Animal Care and Use Committee of the National University of Singapore, and were in compliance with Association for Assessment of Laboratory Animal Care guidelines for animal use. All mice were maintained at C57BL/6J background and housed in groups with individually ventilated cages under a 12:12-h light/dark cycle and access to food/water ad libitum. Because there is no apparent gender bias to the observed phenotypes and pathology, both female and male mice are included and randomly allocated to experimental groups according to age and genotype. No animals or samples were excluded from the experiments.

Conditional TDP-43 (*Tardbp*$^{fl/fl}$) mice (stock no. 017591) were purchased from The Jackson Laboratory. Characterization of *Cnp*-Cre;TDP-43 mice was described previously (Wang et al., 2018). For genotyping, genomic DNA was isolated from tail biopsies using salt extraction methods and subjected to routine PCR methods using the following primers: *Tardbp*$^{fl/fl}$: 5′-CCC TGGCTCATCAAGAACTG-3′ and 5′-TCCAGGACAGCCAGGACT AC-3′; and *Cnp*-Cre: 5′-GGGGATTCCTCAACTGACAA-3′ and 5′-CATGTTTAGCTGGCCCAAAT-3′.

RNA-seq library preparation, sequencing, and bioinformatics analysis

Abundance quantification and differential expression calling

The RNA quality was measured using the Agilent Bioanalyzer system. Samples with RNA integrity numbers >8.0 were used for RNA library preparation. Multiplex strand-specific RNA-seq libraries were prepared from 60-d-old mouse spinal cord RNA using the NEXTflex Rapid Directional RNA-Seq Kit according to manufacturer's instructions. Individual library quality was assessed with an Agilent 2100 Bioanalyzer and quantified with a Qubit 2.0 fluorometer before subsequent sequencing on a HiSeq 2000 using 100-bp single-ended reads. Samples from 21-d-old

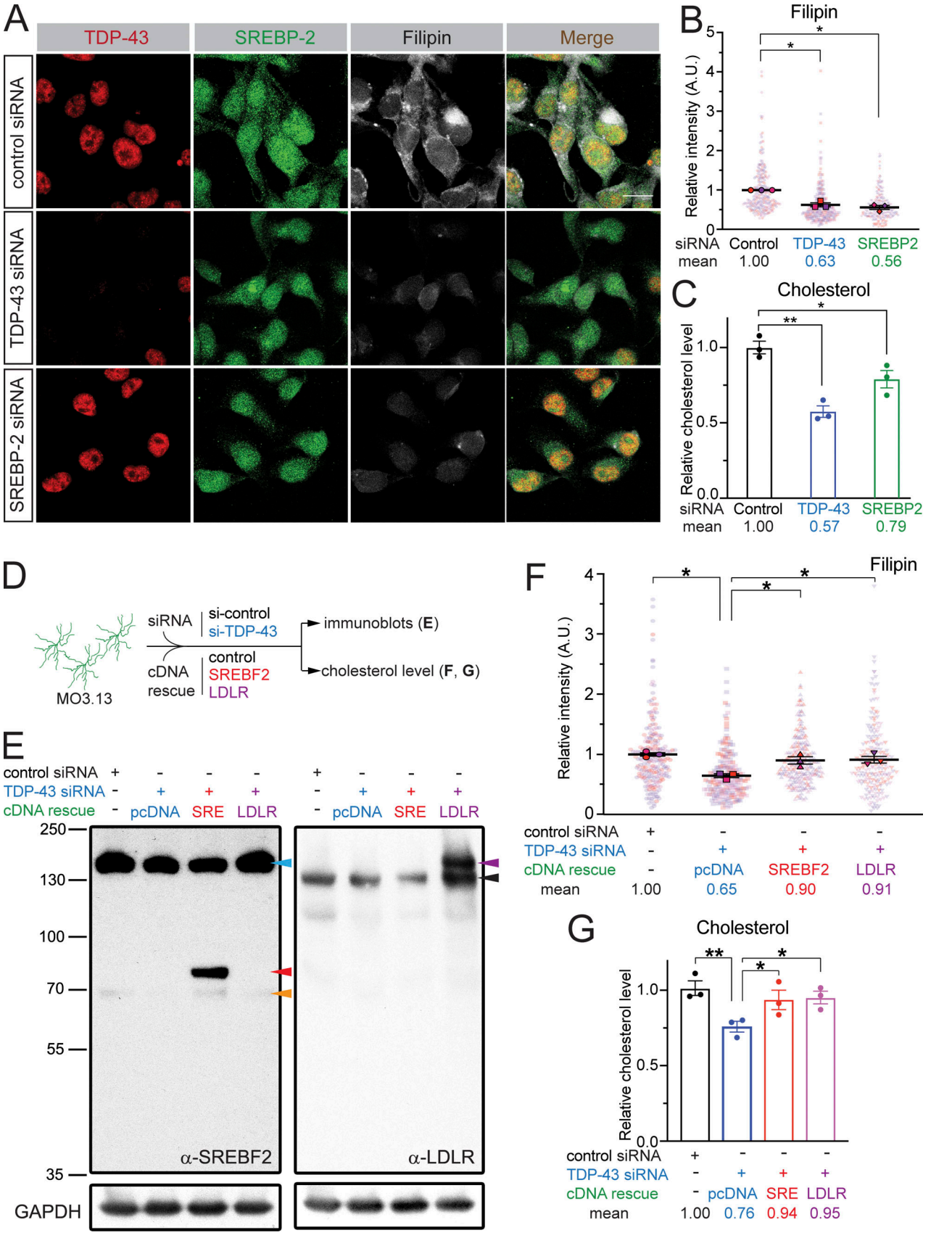

Figure 7. **SREBF2 and LDLR rescue cholesterol reduction caused by TDP-43 deletion. (A)** MO3.13 cells were transfected with control siRNA and siRNA against TDP-43 or SREBF2. Cells were stained with TDP-43 (red), SREBF2 (green), and filipin (gray). Scale bar: 10 µm. **(B)** Relative filipin fluorescent intensity in

cells treated with control siRNA and siRNA against TDP-43 or SREBF2. Quantification was done from three independent experiments with 90 cells quantified per experiment. One-way ANOVA with Tukey's multiple comparisons tests was used to evaluate statistical significance; *, P < 0.05. **(C)** Total cholesterol level as measured by a fluorometric-based assay in cells treated with control siRNA and siRNA against TDP-43 or SREBF2. *n* = 3, one-way ANOVA with Tukey's multiple comparisons tests was used to evaluate statistical significance; *, P < 0.05; **, P < 0.01. **(D)** Schematic of cDNA rescue experiment under TDP-43 knockdown conditions. **(E)** Immunoblotting for SREBF2 and LDLR in the rescue experiments. Blue arrow: full-length SREBF2; red arrow: transfected N-terminal domain of SREBF2; orange arrow: N-terminal domain of SREBF2; purple arrow: GFP-tagged LDLR; black arrow: endogenous LDLR. **(F)** Relative filipin fluorescent intensity in cells treated with control siRNA, or siRNA against TDP-43 with control rescue, or cDNA encoding SREBF2 or LDLR. One-way ANOVA with Tukey's multiple comparisons tests was used to evaluate statistical significance; *, P < 0.05. Quantification was done from at least three independent experiments with 90 cells quantified per experiment. **(G)** Relative cholesterol level as measured by a fluorometric-based assay in cells treated with control siRNA, or siRNA against TDP-43 with control rescue, or cDNA encoding SREBF2 or LDLR. Three independent experiments were performed, and three biological samples were performed per experiment. One-way ANOVA with Tukey's multiple comparisons tests was used to evaluate statistical significance; *, P < 0.05; **, P < 0.01.

spinal cords were prepared using the Illumina TruSeq RNA Sample Prep Kit, and libraries were sequenced using Illumina HiSeq 4000 pair-end 100-bp sequencing. Read quantification was performed with Kallisto (0.43.0) with parameters -b 50 –single -l 200 -s 20 using ENSEMBL cDNA transcripts (release 88). Downstream differential gene expression calling was performed using Sleuth (0.28.1). Here, quantified genes from each sample were annotated with a condition tag corresponding to the sample genotype (*Tardbp*$^{fl/fl}$, *Cnp*-Cre;*Tardbp*$^{fl/+}$ and *Cnp*-Cre;*Tardbp*$^{fl/fl}$). For each gene, Wald testing was performed on the condition parameter to obtain their respective FDR-corrected P values. Significance for each gene was then established using a defined cutoff of FDR <0.1. Sequencing data have been deposited in GEO under accession no. GSE133047.

Diagnostic plot generation

Diagnostic plots (MA, PCA) were generated using the R statistical language. PCA was performed using estimated gene counts generated during the Sleuth differential expression analysis. Gene expression heatmaps were created using expression data for genes that were differentially expressed in either *Cnp-Cre*;*Tardbp*$^{fl/+}$ versus *Tardbp*$^{fl/fl}$ or *Cnp-Cre*;*Tardbp*$^{fl/fl}$ versus Tardbpfl/fl contrasts. Kallisto count estimates for the differentially expressed gene set were log2 scaled and centered in a gene-wise fashion before rendering with the superheat R library.

Visualization of read coverage and CLIP-seq data

Raw read data were mapped against the ENSEMBL mouse genome and associated annotations (release 88) using the STAR aligner package (2.4.2a) with parameters sjdbOverhang = 99. Read coverage of the various datasets was calculated using bedtools genomecov (2.17.0, -bg -split) and rendered alongside *Tardbp* CLIP-seq peaks using the GViz genomic data visualization toolkit (1.20.0).

GO analysis

Selected FDR ordered gene sets were isolated from the *Cnp-Cre*;*Tardbp*$^{fl/+}$ versus *Cnp-Cre*;*Tardbp*$^{fl/fl}$ dataset. The genes were then subjected to GO enrichment using the Cytoscape (3.5.0) package ClueGO (2.3.0) two-sided hypergeometric test with parameters ontology = Biological Process (GO_BiologicalProcess-GOA_23.02.2017_10h01), GO term fusion = True, GOLevels=?? [3, 8]. The resultant network was visualized in Cytoscape under a Bonferroni-corrected P value <0.05 cutoff using the included organic layout. Clusters of interest for downstream analysis were then identified from the network manually.

Cluster gene pathway projection

For each selected cluster, we derived a list of all genes associated with all GO terms contained by the cluster. We then filtered this cluster gene set, removing all genes that were not differentially expressed in the *Cnp-Cre*;*Tardbp*$^{fl/+}$ versus *Cnp-Cre*;*Tardbp*$^{fl/fl}$ analysis. The resultant gene list was then annotated with their respective log2 fold changes and submitted to the Reactome analyzer service for pathway enrichment using a two-sided hypergeometric test. The resultant projection was then visualized using the Reactome pathway browser.

TDP-43 binding partner analysis

TDP-43 binding targets in the chosen gene set were defined by integrating two sources. Primary peak-calls from our previous work (Polymenidou et al., 2011) meeting a FDR cutoff of 0.01 were used. To supplement this, we aggregated TDP-43 CLIP-seq Piranha peak-calls from a total of six mouse datasets from the CLIPdb database (Yang et al., 2015). Here, genes were scored on the number of datasets showing the presence of the gene-RBP interaction, regardless of the number of peaks in the individual datasets. TDP-43 binding sites were then classified by integrating the two sources. High-confidence peaks were peaks with either six or more peaks in the Polymenidou dataset or four-dataset agreement. Moderate-confidence peaks had either two or more peaks or two or more dataset agreement. Low-confidence peaks had at least one peak or appeared in at least one CLIPdb dataset.

RNA extraction and RT-qPCR

Total RNAs were extracted from the spinal cord tissues using TRIzol reagent (Thermo Fisher Scientific) according to the manufacturer's instructions. After DNase treatment using RQ1 RNase-Free DNase (Promega), 1 µg RNA was reverse-transcribed using the Maxima First Strand cDNA Synthesis Kit for RT-qPCR (Thermo Fisher Scientific). mRNA levels were determined using Maxima SYBR Green qPCR master mix (Thermo Fisher Scientific). Primers for genes of interest are listed in Table S1. The expression levels of the genes of interest were normalized to the extended ΔCT, obtained from three reference genes, e.g., RPL13, RPLP0, and ARHGDIA.

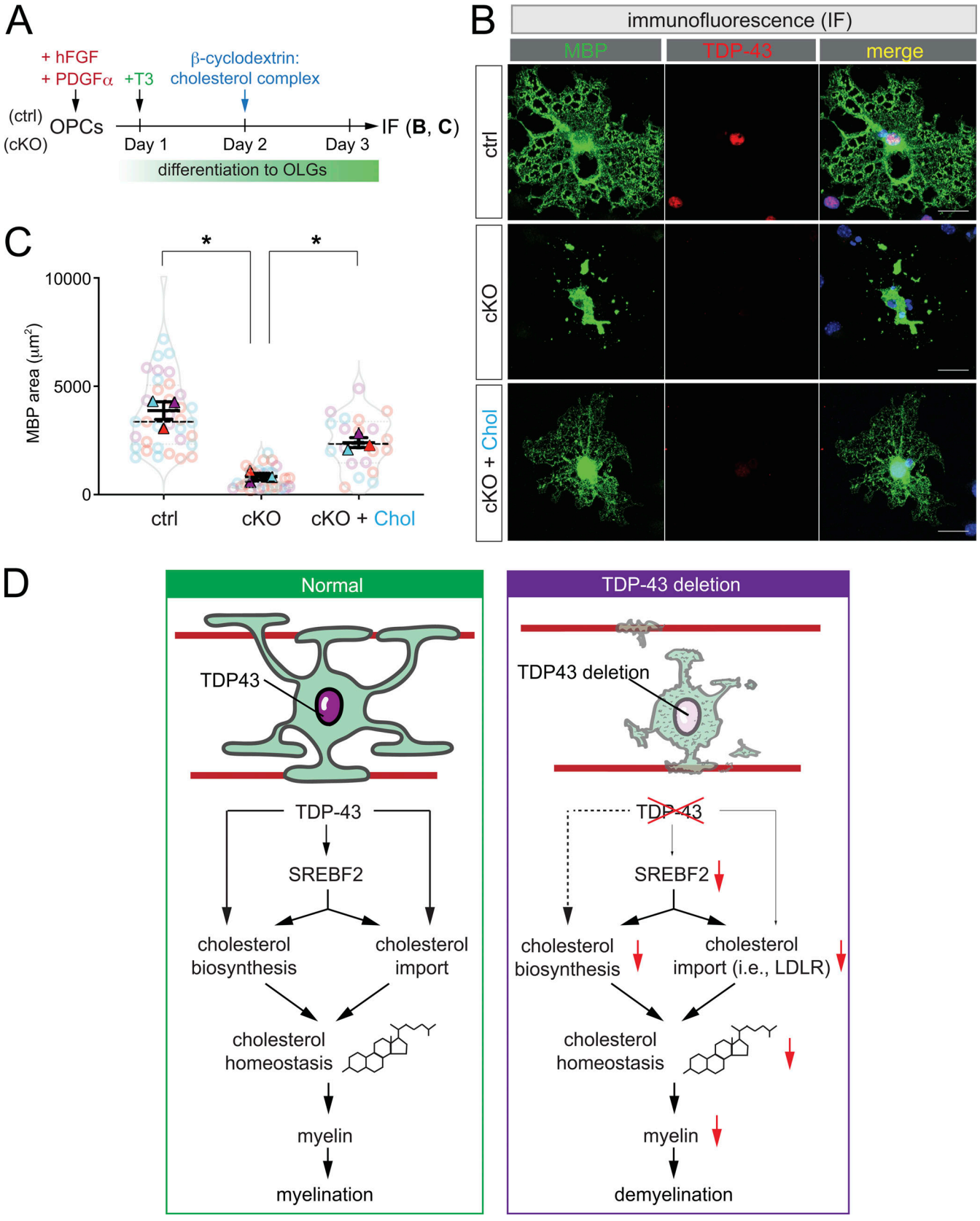

Figure 8. **Cholesterol supplementation reverses myelin status in TDP-43–deleted oligodendrocytes. (A)** Schematic of cholesterol supplementation experiments using primary oligodendrocytes cultured from *Tardbp*$^{fl/fl}$ (ctrl) and *Cnp*-Cre;*Tardbp*$^{fl/fl}$ (cKO) mice. Water-soluble cholesterol (β-cyclodextrin cholesterol complex) was incubated with cKO oligodendrocytes. **(B)** Confocal images of MBP and TDP-43 staining of oligodendrocytes from ctrl, cKO, and cKO with cholesterol supplementation (cKO + Chol). Scale bar is 20 µm. **(C)** Quantification of MBP area in oligodendrocytes from ctrl, cKO, and cKO with cholesterol

supplementation (cKO + Chol). Cholesterol supplementation restores the myelination phenotype caused by TDP-43 deletion. MBP area of individual oligodendrocytes (faded circle), and means (solid triangle) for each set of experiment (n = 3) plotted, total mean ± SEM derived from all sets of experiments. Significance was tested using unpaired t test, *, $P < 0.05$. Quantification was done from three independent experiments with at least 10 cells quantified per experiment. **(D)** Graphic summary and proposed model for how deletion of TDP-43 affects myelin via regulating SREBF2-mediated cholesterol metabolism in the oligodendrocytes. cKO, conditional knockout; ctrl, control.

Immunohistochemistry and image acquisition

Mice were anesthetized with isoflurane and perfused transcardially with PBS, followed by 4% PFA in phosphate buffer for fixation. Spinal cords were dissected and post-fixed in 4% PFA in PBS for 2 h. Tissues were cryopreserved in 30% sucrose for >24 h and embedded in Tissue-Tek before sectioning. Lumbar spinal cords were sectioned at 30 µm using a cryostat or microtome.

For spinal cord section staining, after washing three times with 1× PBS, sections were permeabilized in 0.3% Triton X-100 in 1× PBS for 5 min. The permeabilization steps were repeated twice. Primary blocking buffer containing 5% BSA and 0.5% Tween-20 in 1× PBS was used for blocking and primary antibody incubation. After blocking at RT for 1 h, the sections were incubated with primary antibodies at 4°C overnight. The antibodies used in this study were mouse monoclonal APC (Merck; clone CC1; OP80; 1:200), SREBF2 (Abcam; ab30682; 1:400), LDLR (Proteintech; 10785–1-AP; 1:500), and HMGCS1 (Proteintech; 17643–1-AP; 1:500). Sections were washed with 1× PBS three times for 5 min each. Secondary antibodies conjugated with Alexa Fluor 488, 568, or 647 (Thermo Fisher Scientific; 1:1,000) and 1 µg/ml DAPI were diluted in secondary blocking buffer containing 2% BSA and 0.5% Tween-20 in 1× PBS, and sections were incubated at RT for 1 h in the dark. After incubation, sections were washed and mounted onto slides with Prolong Gold anti-fade reagent (Thermo Fisher Scientific; P36930). Details of primary and secondary antibodies used in this study are listed in Table S2 and Table S3, respectively. Confocal images were acquired with a Zeiss LSM700 inverted confocal microscope with four laser lines (405/488/555/639 nm) with either 20×/0.8 NA air or 63×/1.15 NA oil immersion objectives. Images were captured using an AxioCam MRm monochromatic CCD camera (Zeiss) run by Zeiss Zen software.

Black-Gold II staining

The myelin of brain and spinal cord sections were stained with Black-Gold II aurohalophosphate complex (Merck; AG105) according to the manufacturer's manual.

RNA-FISH, combined RNA-FISH and IF, and quantification of RNA-FISH signals

RNA-FISH

Mice were anesthetized with isoflurane and perfused transcardially with PBS. Spinal cords were dissected and embedded in Tissue-Tek. Fresh frozen lumbar spinal cords were sectioned at 10 µm using a cryostat and mounted onto slides. Sections were dried at −20°C and stored at −80°C until use. For pretreatment, the slides were fixed in prechilled 4% PFA for 15 min at 4°C, dehydrated in 50% EtOH, 75% EtOH, and 100% EtOH sequentially, and air dried for 5 min. A hydrophobic barrier was created around the sections using a hydrophobic barrier pen. RNAscope Protease IV was applied to each section and incubated at RT for 10 min. Slides were washed in 1× PBS twice briefly. RNAscope Fluorescent Multiplex Assay was performed according to the manufacturer's protocol. In brief, pretreated sections were incubated in RNAscope probes C1 (LDLR), C2 (TDP43), and C3 (SREBF2) for 2 h at 40°C to hybridize probes. The sections were incubated in the detection reagents in the following order: Amp 1-FL for 30 min, Amp 2-FL for 15 min, Amp 3-FL for 30 min, and Amp 4 Alt A-FL for 15 min. Finally, sections were counterstained with DAPI and coverslipped with Prolong Gold. Confocal images were acquired with a Zeiss LSM700 inverted confocal microscope with four laser lines (405/488/555/639 nm) with a 20×/0.8 NA air lens at ambient temperature. For each animal, five lumbar spinal cord sections were imaged for quantification. n = 3 per genotype, and at least three sections were quantified per region per animal. Measurement from different sections were averaged for each animal. Two-tailed unpaired t test was used for statistical comparison.

Combined RNA-FISH and IF

Mice were anaesthetized with isoflurane and perfused transcardially with 1× PBS and 4% PFA. Spinal cords were dissected and post-fixed in 4% PFA in PBS for 2 h. Tissues were cryopreserved in 30% sucrose for >24 h before embedding in optimum cutting temperature compound (Leica FSC22 clear frozen section compound) and stored at −80°C until further processing. The lumbar spinal cord was cryo-sectioned at 15 µm, thaw mounted onto charged slides (Trajan Scientific; cat #473042491), and left to air dry at −20°C for 1 h before storing at −80°C. Sections were processed according to the manufacturer's protocol (ACDbio). 1 d before the assay, sections were processed for primary antibody incubation. Sections were washed in 1× PBS, baked at 60°C for at least 30 min, and then fixed with 4% PFA for 15 min at 4°C. Sections underwent dehydration in increasing concentrations, 50%, 70%, and 100%, of ethanol for 5 min each before hydrogen peroxide (ACDbio; cat #322381) treatment at RT for 10 min. After two washes in distilled water, sections were boiled in 1× target retrieval solution (ACDbio; cat #322000) for 5 min and then rinsed with distilled water followed by 0.1% Tween-20 in 1× PBS (PBS-T). Hydrophobic barriers were quickly created around the sections using the ImmEdge hydrophobic barrier marker (Vector Laboratories; PAP pen). Sections were incubated with rabbit anti-GST-P1 (Proteintech; 15902–1-AP; 1:200) diluted in codetection antibody diluent (ACDbio; cat #323160) overnight at 4°C. RNA-FISH was performed the following day. Sections were washed with 1× PBS-T three times for 2 min each and then fixed with 4% PFA at RT for 30 min. After four 2-min washes in PBS-T, sections were incubated with Protease Plus (ACDbio; cat #322381) for 30 min at 40°C. Sections were then washed twice in distilled water before incubation with RNAscope

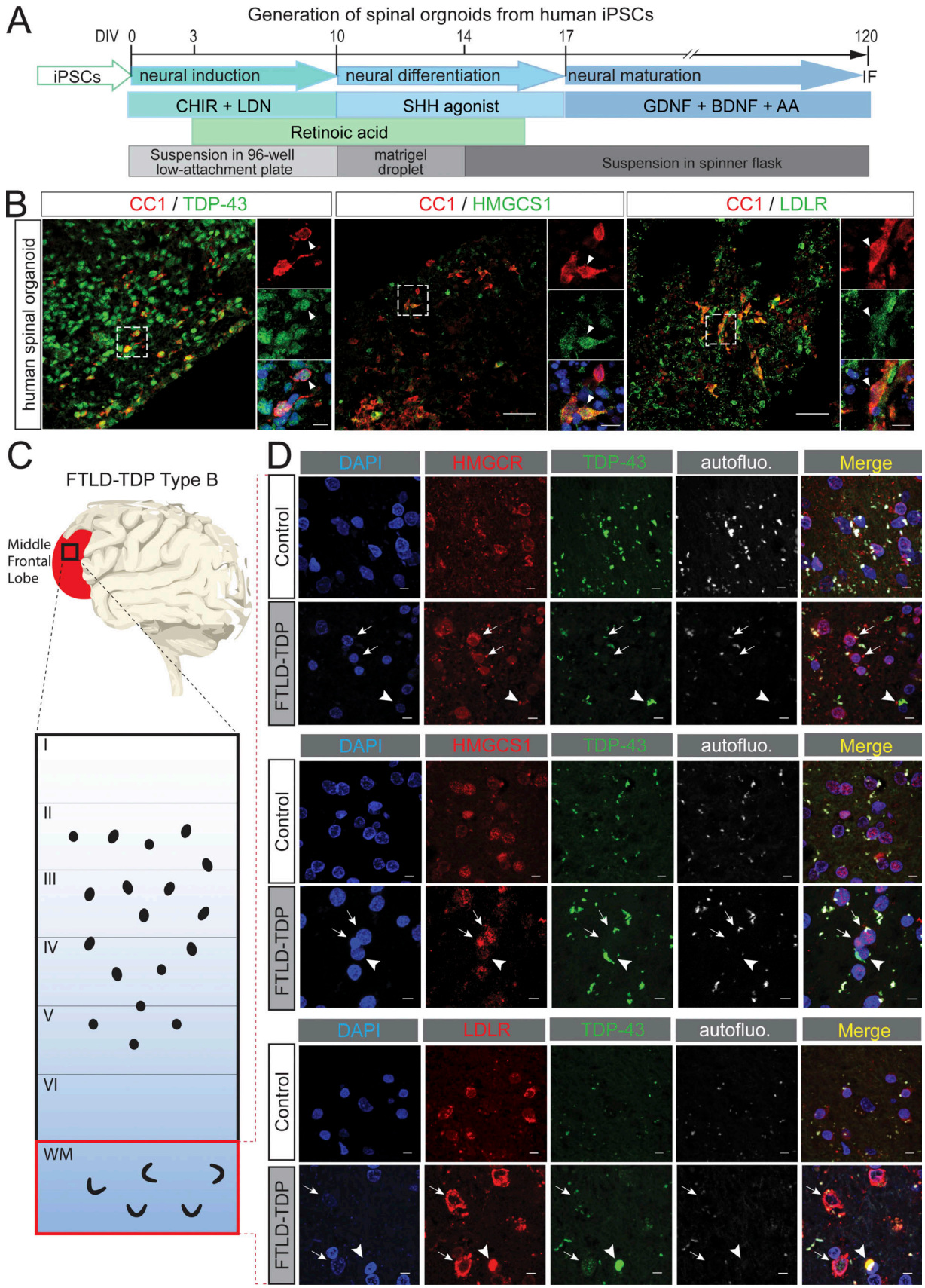

Figure 9. **Reduced expression of cholesterol metabolism in the glia from FTD-TDP patients. (A)** Schematic illustration of spinal organoids differentiation from iPSC. **(B)** Confocal images of TDP-43 (left), HMGCS1 (middle), and HMGCR (right) with mature oligodendrocyte marker (CC1). DAPI nuclear stain in blue.

Enlarged images show TDP-43, HMGCS1, and LDLR1 with oligodendrocytes. Scale bar = 50 µm. For magnified images, scale bar = 10 µm. **(C)** Schematic of post-mortem human FTLD-TDP tissues used for this study. **(D)** Double IF shows cytoplasmic TDP-43 inclusions (green) associated with white matter oligodendrocytes. Oligodendrocytes with TDP-43 inclusions appear to show a decrease in HMGCR (top, red, arrowheads) and HMGCS1 (middle, red, arrowheads) staining compared with other glial cells (arrows). LDLR colocalizes with TDP-43 inclusions (bottom, red). DAPI nuclear counterstain is blue. White image was taken using 561-nm excitation and corresponds to autofluorescence (autofluo.). Scale bar = 5 µm. DIV, days in vitro; SHH, Sonic Hedgehog; AA, ascorbic acid; WM, white matter.

probe mixture (ACDbio; Mm-Ldlr-C1; cat #443701; or ACDbio; Mm-Srebf2-C3; cat #562261-C3; or ACDbio; Mm-Tardbp-C2; cat #518961-C2) at 40°C for 2 h. After probe incubation, slides were rinsed twice with 1× wash buffer (ACDBio; cat #310091) at RT for 2 min each. Signal amplification was achieved through multiple sequential incubations using RNAscope Multiplex Fluorescent Detection Reagents V2 (ACDbio; cat #323110) at 40°C as follows: AMP1 for 30 min, AMP2 for 30 min, and AMP3 for 15 min. Finally, signal was developed by means of HRP/tyramide signal amplification–mediated enzymatic reactions through sequential incubations at 40°C with channel-specific conjugated HRP for 30 min, opal dye (Akoya Biosciences) diluted in tyramide signal amplification buffer (ACDbio; cat #322809) for 30 min, and then HRP blocker (ACDbio; cat #323110) for 15 min, with two 2-min washes with 1× wash buffer between each step. This reaction was repeated for each probe channel, with specific opal dyes (Opal-520 for Ldlr or Tardbp, and Opal-690 for Srebf2). After two final washes in 1× wash buffer, sections were rinsed in PBS-T and then left in donkey anti-rabbit IgG tagged with Alexa Fluor 568 (Thermo Fisher Scientific; cat #A10042; 1:1,000) diluted in codetection antibody diluent (ACDbio; cat #323160) for 1 h at RT. Following two washes in PBS-T, DAPI was applied for 30 s at RT before coverslipping with ProLong Gold mounting media (Thermo Fisher Scientific). Slides were left to dry in the dark at RT before storing at 4°C. Z-stacked images were acquired using a Zeiss LSM700 inverted confocal microscope with four laser lines (405/488/555/639 nm) at 20× magnification, 0.8 NA air lens at ambient temperature. For each animal, five lumbar spinal cord sections were imaged for quantification using IMARIS (Bitplane, version 9.5).

Quantification of RNA-FISH signals

For each spinal section, 10 cells positive for both DAPI and glutathione S-transferase Pi 1 were selected as oligodendrocytes within the ventral white matter of the lumbar spinal cord. Selected oligodendrocytes were then analyzed for LDLR and SREBF2 mRNA expression in 3D. Oligodendrocytes were reconstructed in 3D from Z-stacked confocal images using the *surface creation* tool with manual thresholding and a surface smooth detail of 0.6 µm using Imaris software (Oxford Instruments). Oligodendrocytes were individually cropped before performing *spots* analysis. Spots representative of individual mRNA puncta for LDLR and SREBF2 were created using the *spots* function, with manual thresholding, background subtraction, and an estimated spot diameter of 0.7 µm. Point spread function along the z axis was corrected for 1.4 µm. Only spots rendered within the 3D boundaries of each oligodendrocytes were quantified. n = 3 per genotype, five sections were quantified per animal, 10 cells were counted per section. Measurement from different cells were averaged for each animal. Two-tailed unpaired t test was used for statistical comparison.

Primary OPC culture, oligodendrocyte differentiation, RNA-FISH, IF, immunoblots, and cholesterol restoration

Primary OPC culture from mouse spinal cords was isolated from P7 mouse pups based on the immunopanning protocol. In brief, spinal cord tissues were diced with a sterile scalpel blade and incubated at 37°C for 20 min in papain solution (Sigma-Aldrich; 20 U/ml). The tissue was then triturated sequentially in a solution containing ovomucoid (Worthington). Cell suspension was filtered through a nylon cell strainer (70 µm pore size). The filtered cell suspension was first placed on a lectin (Vector Laboratories; *Bandeiraea simplicifolia* lectin 1 [BSL1])–coated plate for 15 min at RT. The nonadherent cells were transferred to the second BSL1 plate for 15 min. Afterward, the nonadherent cells were transferred to the anti-Mouse CD140a (BD Pharmingen)–coated plate for 45 min, with brief and gentle agitation every 15 min. The plate containing CD140a$^+$ OPCs was washed eight times with 10 ml of Dulbecco's phosphate-buffered saline with Mg^{2+} and Ca^{2+} (Gibco) with agitation to remove all antigen-negative nonadherent cells. Adherent cells were incubated in 5 ml of trypsin/Earle's Balance Salts (Sigma-Aldrich; 1,000 U/ml) for 5 min at 37°C in a 5% CO_2 incubator. The cells were then gently dislodged using DMEM high glucose (Thermo Fisher Scientific) and centrifuged at 1,200 rpm for 10 min. The pelleted cells were then resuspended in SATO (2 mg apo-transferrin, 2 mg BSA, 0.32 mg putrescine, 1.25 µg progesterone, 0.8 µg sodium selenite in DMEM) medium containing bovine insulin (Sigma-Aldrich; 50 µg/ml), N-acetyl-cysteine (Sigma-Aldrich; 50 µg/ml), forskolin (Sigma-Aldrich; 5 nM), trace element B (Cellgro), penicillin-streptomycin (Biowest), L-glutamine (Invitrogen), sodium pyruvate (Invitrogen), B27 supplement (Invitrogen), and SATO stock (Apo-transferrin, progesterone, and sodium selenite) in DMEM, and cultured on poly-D-lysine (Sigma-Aldrich; 0.1 mg/ml)–coated glass coverslips in 24-well plates. Human PDGF-AA (Peprotech; 10 ng/ml) and human bFGF (Peprotech; 10 ng/ml) were added to the culture every day for proliferation for 7 d. PDGF and bFGF were replaced with T3 (Peprotech; 40 ng/ml) for oligodendrocyte differentiation for 3 d.

IF

Cells were fixed on the third day in 4% paraformaldehyde supplemented with 4% sucrose in 1× PBS. Fixed cells were washed once with PBS followed by 20 mM glycine (Sigma-Aldrich). Cells were permeabilized in 0.3% PBS-T and blocked in 5% donkey serum in 0.3% PBS-T. Primary antibodies were prepared in 1% donkey serum in PBS and incubated overnight at 4°C. The primary antibodies used in this study were SREBF2 (Abcam; ab30682; 1:200), MBP (Merck; MAB386; 1:500), LDLR (Proteintech; 10785-1-AP; 1:500), and TDP43 (clone FL4; in-house [Ling et al., 2010]; 1:500). Cells were then washed with PBS three times and incubated in

secondary antibodies at RT for 1 h. The secondary antibodies used were donkey anti-rabbit IgG Alexa Fluor 568 conjugate (Thermo Fisher Scientific; A10042), donkey anti-mouse IgG Alexa Fluor 647 conjugate (Thermo Fisher Scientific; A31571), and donkey anti-rat IgG Alexa Fluor 488 conjugate (Thermo Fisher Scientific; A21208). After the addition of 1 µg/ml DAPI, cells were washed three times in PBS and mounted with ProLong Gold antifade reagent (Thermo Fisher Scientific). A Zeiss LSM700 inverted confocal microscope and a 63×/1.15 NA oil immersion objective were used for visualization and image acquisition.

RNA-FISH

Cells were fixed on the third day in prechilled 4% paraformaldehyde for 15 min at 4°C before being dehydrated in 50% EtOH, 75% EtOH, and 100% EtOH sequentially. RNAscope Protease III was applied to each coverslip and incubated at RT for 30 min. Coverslips were washed in 1× PBS twice. RNAscope Fluorescent Multiplex Assay was performed according to the manufacturer's protocol. In brief, pretreated sections were incubated in RNAscope probes C1 (LDLR), C2 (TDP-43), and C3 (SREBF2) for 2 h at 40°C to hybridize probes. The sections were incubated in the detection reagents in the following order: Amp 1-FL for 30 min, Amp 2-FL for 15 min, Amp 3-FL for 30 min, and Amp 4 Alt A-FL for 15 min. Finally, sections were counterstained with DAPI and coverslipped with Prolong Gold. Confocal images were acquired with a Zeiss LSM700 inverted confocal microscope with four laser lines (405/488/555/639 nm) with a 20×/0.8 NA air lens at ambient temperature. Three independent sets of cultures (n = 3) were performed. At least 10 cells were imaged per coverslip per genotype for each set of experiments. Measurements from different cells were averaged for each set of experiment. Two-tailed unpaired t test was used for statistical comparison.

Immunoblotting

Cells were lysed on the third day in RIPA buffer (150 mM NaCl, 1% Triton X-100, 0.5% sodium deoxycholate, 0.1% SDS, and 50 mM Tris, pH 8.0) supplemented with protease inhibitor cocktails and incubated at 4°C for 20 min with gentle agitation. After incubation, lysed samples were centrifuged at 4°C for 15 min at 13,500 ×g using a benchtop centrifuge. Supernatant was collected for bicinchoninic acid (BCA) protein concentration measurement (Thermo Fisher Scientific; 23225). 20 µg of total protein for each sample was loaded for 8% Bis-Tris gel. Proteins were transferred to polyvinylidene fluoride membrane using 1× transfer buffer containing 1× Tris-glycine (25 mM Tris base and 192 mM glycine) and 20% methanol at 100 V for 1 h. Membranes were blocked using 5% milk in 1× 50 mM Tris, 150 mM NaCl, and 0.1% Tween 20, pH 7.4 (TBST) at RT for 1 h. After blocking, membranes were incubated with primary antibodies at 4°C overnight. The primary antibodies used in this study were mouse monoclonal MBP (Millipore; MAB386; 1:2,000), GAPDH (Proteintech; 60004-1-Ig; 1:5,000), HMGCS1 (Proteintech; 17643-1-AP; 1:1,000), and LDLR (Proteintech; 10785-1-AP; 1:1,000). Membranes were washed with 1× TBST and incubated with appropriate HRP-conjugated secondary antibodies (Thermo Fisher Scientific; 1:1,000) at RT for 1 h. After washing with 1× TBST extensively, target proteins were probed using SuperSignal West Pico or Femto Chemiluminescent Substrate (Thermo Fisher Scientific).

Cholesterol supplementation

For cholesterol restoration, when cells were ∼60–70% confluent, PDGF and bFGF were replaced with T3 (Peprotech; 40 ng/ml) to start oligodendrocyte differentiation on day 1. On the subsequent day, cells were treated with 0.1 mM water-soluble cholesterol (Sigma-Aldrich; C4951) in T3 media for 30 min at 37°C, 5% CO_2. Cells were briefly washed once with 1× PBS and replaced with fresh T3 media. On day 4, cells were fixed with 4% PFA/4% sucrose for 20 min at RT and stored at 4°C. The primary antibodies used in this experiment were MBP (Merck; MAB386; 1:500) and TDP43 (clone FL4; in-house [Ling et al., 2010]; 1:500). A Zeiss LSM700 inverted confocal microscope and a 63×/1.15 NA oil immersion objective were used for visualization and image acquisition at ambient temperature. At least 10 cells were imaged per coverslip per genotype for each set of experiments (n = 3). Measurements from different cells were averaged for each set of experiments. Two-tailed unpaired t test was used for statistical comparison.

UV CLIP and RT-PCR

UV cross-linking coupled with immunoprecipitation was modified from previously described procedures (Polymenidou et al., 2011; Chang et al., 2014) and detailed below. To maintain protein–RNA interactions, MO3.13 cells were harvested with cell scrapers in ice-cold PBS and exposed to 200 mJ of UV irradiation three times on ice. Cells were centrifuged at ∼600 ×g for 5 min at 4°C, and the supernatants were removed. The cell pellets (∼10^6 cells) were lysed in 600 µl Tris lysis buffer (50 mM Tris-HCl to pH 7.5, 150 mM NaCl, 1% Triton X-100, 1 mM EDTA, 5% glycerol, 2 mM AEBSF (4-(2-aminoethyl)benzenesulfonyl fluoride hydrochloride), 0.3 µM aprotinin, 130 µM pepstatin, 14 µM E-64, 1 µM leupeptin, and 1 U/µl SUPERase-In RNase inhibitor). The lysates were kept on ice for 30 min and centrifuged at 15,000 ×g. The supernatants were split into two parts: one part was treated with 4 µg/ml anti-TDP-43 antibodies (ProteinTech; 12892-AP), and the rest was for control treatment (Sigma-Aldrich; 4 µg/ml rabbit IgG) in low DNA-binding tubes (Eppendorf). The supernatants-antibodies mixtures were incubated on a rocker at 4°C for 1 h. Protein-G agarose (Santa Cruz Biotechnology; 40 µg) was added to the lysates and incubated for an additional 2 h at 4°C, followed by washing three times with lysis buffer. The final immunoprecipitants were separated into two parts: one used for RNA extraction and the other used for immunoblot detection to determine the TDP-43 recovery efficiency. Samples for RNA extraction were treated with protease K (Promega; 100 µg/ml) for 30 min at 37°C, and RNAs were subsequently isolated with TRIzol (Thermo Fisher Scientific) and precipitated with coprecipitant, GlycoBlue (Thermo Fisher Scientific). Total RNAs were treated with DNase (Promega) and reverse-transcribed using SuperScript III (Thermo Fisher Scientific) with random hexamers. The cDNA was PCR-amplified with the primers for TDP-43, SREBF2, HMGCS1, HMGCR, LDLR, and diphosphomevalonate decarboxylase (MVD) with the following conditions: 95°C for 2 min, followed by 32 cycles of 30 s at 95°C, 20 s at 60°C, and 40 s at 72°C, and a final incubation at 72°C for 5 min. PCR primers are listed in Table S1.

Cell culture, siRNA treatment, cDNA rescue, and immunoblotting

The MO3.13 cell line was maintained in DMEM (Thermo Fisher Scientific; 11885–084) with 5% FBS (Hyclone) and 1% Pen/Strep (Gibco) at 37°C and 5% atmospheric CO_2. To mimic the normal physiological glucose concentration in the CNS (Cheng et al., 2015), glucose concentration was reduced gradually from 25 mM to 5 mM. siRNA for TDP-43 was validated previously (Polymenidou et al., 2011) with the following sequence: 5′-CAC UACAAUUGAUAUCAAA-3′. SMARTpool siRNAs for human SREBF2, LDLR, HMGCS1, and HMGCR were purchased from Dharmacon with the following sequences: SREBF2: (1) 5′-GGA CAGCGCUCUGGCAAAA-3′, (2) 5′-GCACACUGGUUGAGAUCCA-3′, (3) 5′-GCAGUGUCCUGUCAUUCGA-3′, and (4) 5′-GAAAGG CGGACAACCCAUA-3′; HMGCS1: (1) 5′-CAUAGCAACUGAGCA UAUU-3′, (2) 5′-GGAACGUGGUACUUAGUUA-3′, (3) 5′-GAACAG AGACAAUCAUCGA-3′, and (4) 5′-UUACAAGCCUGUAUGCUA-3′; HMGCR: (1) 5′-GUGAGAAUGUUAUUGGAUA-3′, (2) 5′-GGU CGAAGAUCAAUUUACA-3′, (3) 5′-GAACAAGUUAUUACCCUAA-3′, and (4) 5′-GAGCAGUGACAUUAUAAUU-3′; and LDLR: (1) 5′-GGACAGAUAUCAUCAACGA-3′, (2) 5′-GAUGAAGUUGGCUGC GUUA-3′, (3) 5′-GUGCAUCUCUCGGCAGUUC-3′, and (4) 5′-GCA AUGACCUUAAGAUCGG-3′. Non-targeting control siRNA sequence was 5′-AAUUCUCCGAACGUGUCACGU-3′. For siRNA treatment, 2 × 10^5 of MO3.13 cells/well were seeded in 6-well plates supplemented with DMEM (Thermo Fisher Scientific) and 10% FBS 1 d before transfection. Control siRNA, TDP-43 siRNA, or SREBF2 siRNA, cDNA plasmids encoding SREBF2 (Addgene; cat #26807) and LDLR (Addgene; cat #98184), were transfected using DharmaFECT 1 and Lipofectamine 2000 transfection reagent according to the manufacturer's instructions. 24 h after transfection, the medium was replaced by fresh culture medium consisting of DMEM and 10% FBS. 72 h after siRNA transfection, cells were lysed in Tris lysis buffer, and total proteins were quantified using BCA protein assay (Thermo Fisher Scientific; 23225) and solubilized in SDS-PAGE sample loading buffer. The proteins were separated by molecular weight with Tris-glycine SDS-PAGE and transferred to the nitrocellulose membrane (Bio-Rad). The membranes were stained with Ponceau S for visualization of the total protein inputs and blotted with the following primary antibodies: TDP-43 (Proteintech; 10782–2-AP; 1:1,000), SREBP2 (Abcam; ab30682; 1:1,000), LDLR (Proteintech; 10785–1-AP; 1:1,000), and GAPDH (Proteintech; 60004-Ig; 1:10,000), for verification of the efficiency of siRNA treatments and the level of rescue constructs. For SREBP2 protein level quantification, films were scanned and converted into electric files and quantified using software ImageJ. Three independent experiments were performed, and three biological samples were performed per experiment. Statistical analysis was performed by a one-way ANOVA test.

Cell lysates were prepared in ice-cold Tris lysis buffer, and immunoblotting was performed as described in the section "UV CLIP and RT-PCR." For IF, cells were washed in PBS and fixed with 4% PFA for 15 min after the indicated siRNA treatment. Cells were permeabilized with 0.1% Triton-X in PBS for 10 min. The following primary antibodies were used: SREBF2 (Abcam; ab30682; 1:500) and TDP-43 (FL4; in-house [Ling et al., 2010]; 1:500). The primary antibodies were diluted in blocking buffer containing 5% goat serum and 1% BSA in PBS with 0.05% Tween-20 and incubated overnight at 4°C. Fluorescent secondary antibodies, donkey anti-rabbit IgG Alexa Fluor 488 conjugate (Thermo Fisher Scientific; A21206), and donkey anti-mouse IgG Alexa Fluor 568 conjugate (Thermo Fisher Scientific; A10037) were diluted in blocking buffer and incubated for 1 h at RT. The cells were rinsed in PBS-T (0.2% Tween-20) and mounted using Prolong Gold (Thermo Fisher Scientific).

Antibody validation

To verify the antibody specificity, transient expression of the targeted proteins (full-length human SREBP2: Addgene cat #26807; full-length human HMGCS1: in-house; full-length human HMGCR: Addgene cat #86085; GFP-tagged full-length human LDLR: Addgene cat #98184), or gene knockdown using the SMARTpool siRNAs mentioned above. In brief, MO3.13 cells were seeded in the 6-well plates 1 d before transfection. The next day, the cells were transfected with the plasmids or the SMARTpool siRNAs by the use of Lipofectamine 2000. The cells were placed in a 37°C incubator for 72 h, with the daily medium changing. The cells were then harvested and lysed in RIPA buffer. To verify the antibody specificity and localization, gene was knockdown using the SMARTpool siRNAs mentioned above. In brief, HeLa cells were seeded on 12-mm glass coverslips. The next day, the cells were transfected with SMARTpool siRNAs by the use of DharmaFECT 1. The cells were placed in a 37°C incubator for 48 h, with a change of media after 24 h. The cells were then fixed with 4% PFA/4% sucrose. IF was performed as mentioned above with the following primary antibodies: SREBP2 (Abcam; ab30682; 1:200), LDLR (Proteintech; 10785–1-AP; 1:500), HMGCS1 (Proteintech; 17643–1-AP; 1:1,000) and HMGCR (Proteintech; 13533–1-AP; 1:500).

RNA half-life

To determine the RNA stability of SREBF2, HMGCR, and LDLR, we adopted and modified the procedures as described previously (Ratnadiwakara et al., 2018). In brief, the cells were transfected with either nontargeted control siRNA or the one against TDP-43 and kept in 37°C with medium changing daily. The 0 h cells were harvested using cell lifter, washed with PBS, and then resuspended with 1 ml TRIzol and were kept at −80°C. For the 2- and 4-h time points, the cells were treated with 5 µg/ml actinomycin D in DMEM low glucose (1 g glucose/liter) medium. Cells were collected accordingly and were resuspended in 1 ml TRIzol. Total RNAs were then isolated from the collected samples and were reverse-transcribed using the Maxima First-strand cDNA Synthesis Kit (Thermo Fisher Scientific; K1671). The targeted gene expression levels were determined by the use of QuantStudio 6 Flex. The exported Ct values were used to calculate the average of replicates for each reaction. We then normalized the Ct average of each time point to the Ct average value of t = 0 to obtain a ΔCt value and the relative abundance for each time point (mRNA abundance = 2[−ΔCT]).

Transcription rate assessment

We adapted the previously described procedure by Singh and Padgett (2009) to assess the transcription rate of SREBF2 and

LDLR. In brief, MO3.13 cells were treated with either nontargeted control siRNA or siRNA against TDP-43 for 72 h at 37°C. The cells were then incubated with 100 µM DRB, a reversible inhibitor for P-TEFb, for 3 h. Subsequently, DRB-containing medium was removed and replaced with the normal complete medium. The cells were collected in 15-min intervals after the removal of DRB (0, 15, 30, and 60 min). Isolation of the total RNAs and reverse transcription were performed as described above. For detecting the newly synthesized transcript, primer pairs against the first exon–intron junction for both *Srebp2* and *Ldlr* were thus applied in the preamplification of the cDNAs, and subsequently, the levels of preamplified cDNAs were evaluated by the nested quantitative PCR. The expression values are all calculated relative to the "no-treatment" control, which was set to 1 for all the sample sets (Singh and Padgett, 2009). At least two independent experiments were performed, and three biological samples were performed per experiment. Statistical analysis was performed by a one-way ANOVA test.

Assessment of translation with puromycin

For the protein translation assessment, a puromycin-based assay, also known as the SUnSET assay, was used (Schmidt et. al, 2009). MO3.13 cells were treated with either nontargeted control siRNA or siRNA against TDP-43 for 72 h at 37°C. The cells were treated with 100 µg/ml puromycin and harvested in 15-min intervals (0, 15, and 30 min). The harvested cells were lysed in lysis buffer (50 mM Tris-HCl, pH 7.5, 150 mM NaCl, 1% Triton X-100, 1 mM EDTA, 5% glycerol, 2 mM AEBSF (4-(2-aminoethyl) benzenesulfonyl fluoride hydrochloride), 0.3 µM aprotinin, 130 µM pestatin, 14 µM E-64, and 1 µM leupeptin), and incubated on ice for 30 min. The lysates were spun at 12,000 ×*g* for 15 min. The supernatants were collected and transferred onto the nitrocellulose membrane by Bio-Dot microfiltration apparatus (Bio-Rad). The membrane was blocked for 30 min in 5% nonfat milk/1× TBST before incubating with primary antibodies against puromycin (Millipore; MABE343; clone 12D10; 1:2,000) or GAPDH (as loading control; Proteintech; cat #60004-1-Ig; 1:5,000). The chemiluminescence signals were obtained as described above. The total protein synthesis rate was calculated as puromycin signal normalized to GAPDH. Furthermore, to test whether TDP-43 affects protein synthesis of SREBP2 and LDLR, the lysates were incubated with the anti-puromycin antibody-coupled beads overnight at 4°C. The protein–antibody–bead complexes were spun at 12,000 ×*g* for 5 min, followed by supernatant removal and lysis buffer wash three times. The immunoprecipitated proteins were eluted in SDS loading buffer, transferred onto the membranes by Bio-Dot microfiltration apparatus (Bio-Rad), and probed with LDLR (Proteintech; 10785-1-AP; 1:1,000) antibody. The chemiluminescence signals were obtained as described above. Three independent experiments were performed, and two biological samples were performed per experiment. Statistical analysis was performed by a one-way ANOVA test.

Filipin, cholesteryl BODIPY-FL C_{12}, BODIPY-493/503, and Nile Red staining, image acquisition, and quantification

MO3.13 cells were plated at 40% confluency on sterile glass coverslips 1 d before transfection. Cells were transfected with siRNAs against TDP-43 or SREBP2 as described and were kept in 37°C for 4 d, with daily medium changes before staining. For filipin staining, cells were rinsed with PBS and fixed in 3% formaldehyde at RT for 1 h. Cells were rinsed with 1× PBS after the fixation and stained with filipin working solution (Sigma-Aldrich; 0.05 mg/ml in PBS plus 10% FBS) for 2 h at RT, followed by PBS washes. For BODIPY 493/503 (Thermo Fisher Scientific; D-3922) and Nile Red staining, we followed the lipid droplet protocol as described (Listenberger and Brown, 2007). In brief, cells were washed with PBS, followed by 3% formaldehyde fixation for 20 min at RT, and PBS washes. Cells were stained with either BODIPY 493/503 (1 µg/ml in 150 mM NaCl) or Nile Red (0.1 µg/ml in 150 mM NaCl) for 10 min at RT, followed by 1× PBS washes. For cholesteryl BODIPY-FL C_{12} (Thermo Fisher Scientific; C-3927) staining, cells were incubated with 5 µM of this molecule in culture medium for 4 h at 37°C, followed by PBS washes, 3% formaldehyde fixation for 30 min, and then PBS washes. All samples were mounted with ProLong Gold antifade reagent (Thermo Fisher Scientific). Confocal images were acquired with a Zeiss LSM700 inverted confocal microscope with four laser lines (405/488/555/639 nm) with a 63×/1.15 NA oil immersion objective. Images were captured using an AxioCam MRm monochromatic CCD camera (Zeiss) run by Zeiss Zen software. To quantify the fluorescence within the cells, we used the built-in "Threshold" function in ImageJ to outline the cells and then quantify the mean and area of the fluorescence within the cells, along with the adjacent background recording. For all the treatments mentioned, at least three independent sets were performed with 30–50 cells counted per set of >120 cells counted per treatment.

Cholesterol measurement from cell culture

The total cholesterol contents, including cholesteryl ester, were determined by a fluorometric-based assay (Merck-Millipore; 428901) according to the manufacturer's manual. In brief, 1×10^6 cells were homogenized in 400 µl chloroform:isopropanol:NP40 (7:11:0.1) by a micro-homogenizer. The samples were then centrifuged at 16,000 ×*g* for 10 min. The organic phases were transferred to clean tubes and were air dried at 50°C. The lipid-cholesterol mixtures were resuspended in the cholesterol assay buffer (Merck-Millipore; 427901). The fluorometric signal was determined using a plate reader (BioTek). The cholesterol levels were calculated with a standard curve of cholesterol and normalized to those of control treatment. Three independent experiments were performed, and three biological samples were performed per experiment. Statistical analysis was performed by a one-way ANOVA test.

Cholesterol and PC measurements from mouse tissues

Sample preparation

The frozen spinal cord samples were lyophilized until a constant weight was obtained. PBS was added to each sample in proportion to its respective dry weight (30 µl per mg) and homogenized with Omni beadruptor homogenizer (Omni International) with the following settings: speed 5.15 m/s, six cycles, 45 s for each cycle, with 10 s dwell time. A quality control sample was prepared by pooling aliquots from each homogenate.

Lipid extraction

Lipid extraction from homogenates was done according to the method of Bligh and Dyer (1959). Briefly, 180 µl of freshly prepared and chilled chloroform/methanol ($CHCl_3$/MeOH) 1/2 vol/vol (Thermo Fisher Scientific) containing PC 28:0 or cholesterol-d_6 as internal standards (Avanti Polar Lipids) were added to 10 µl of homogenate. Samples were vortexed and then incubated with agitation on a thermomixer at a speed of 700 rpm at 4°C in the dark for 1 h. Organic phases were transferred to new tubes, and the homogenates were reextracted with 500 µl of chilled $CHCl_3$. The organic phases were combined and dried in a vacuum concentrator. Dried lipid extracts were dissolved in 100 µl of $CHCl_3$/MeOH 1:1 (vol/vol) and stored at −80°C until MS analysis.

Derivatization of cholesterol for GC/MS analysis

A mixture of N-methyl-N-trifluorotrimethylsilyl acetamide/ammonium iodide/dithioerythritol (Sigma-Aldrich; 500/4/2 vol/wt/wt) was added to the dried lipid extracts, followed by incubation at 60°C for 20 min. This solution was used directly for GC/MS analysis after cooling down to RT (Son et al., 2014).

Cholesterol measurement by GC/MS

Cholesterol levels of the samples were measured with an Agilent 7890A GC coupled with an Agilent 7000 Triple Quadrupole MS. Cholesterol was measured in selected ion monitoring, monitoring *m/z* 129.1, *m/z* 329.4, *m/z* 353.4, *m/z* 368.3, and *m/z* 458.5 as characteristic ions for derivatized cholesterol, and corresponding deuterated internal standard ions (*m/z* 135.1, 335.3, 359.3, 374.3, and 464.4). Among the characteristic ions, *m/z* 329.3 and *m/z* 368.3 were used as quantifier and qualifier, respectively. The column used in this experiment was a Phenomenex, Zebro-5HT Inferno, length 30 m, internal diameter 0.32 mm, thickness 0.10 µm. Pressure was 9.0656 psi, flow 1.5 ml/min, average velocity 47.759 cm/s, and holdup time 1.0469 min. The instrument system was setup as follows: source temperature 250°C, electron energy 70 eV, resolution unit, and dwell time 50 s. Injection volume was 1 µl, splitless. The column temperature gradient was as follows: initial set point 220°C, hold for 3 min; 5°C.min^{-1} to 310°C, hold for 3 min; and then 30°C.min^{-1} to 380°C, hold for 3 min, with a total run time of 29.3 min. Quality controls and blanks were injected at regular intervals to monitor stability of the instrument response and carryover. Cholesterol intensities were then normalized to internal standard and protein content and intensities in *Tardbp*$^{fl/fl}$ samples.

PC measurement by liquid chromatography–tandem MS

PC levels were measured with a liquid chromatography–tandem MS instrument (Agilent Technologies; 1290 Liquid Chromatography System and 6460 Triple Quadrupole). Quality controls and blanks were injected after every eight sample injections to monitor the stability of the instrument response and carryover. The chromatographic column was a Kinetex HILIC (Phenomenex; 150 × 2.1 mm, 2.6 µM, 100 Å). Gradient elution was undertaken with solvents A (50% acetonitrile/50% 25 mM ammonium formate buffer, pH 4.6) and B (95% acetonitrile/5% 25 mM ammonium formate buffer, pH 4.6), with a gradient range from 75% to 25% solvent B in 6 min, 90% to 10% solvent B in 1 min, and 0.1% to 99.9% solvent B in 0.1 min, followed by 0.1% to 99.9% solvent B for 3 min (total run time of 10.1 min). PC was quantified at the sum composition level, using multiple reaction monitoring with precursor to headgroup transitions (precursor → *m/z* 184). In total, 46 PC species were measured in the samples. MS parameters were as follows: gas temperature 300°C, gas flow 5 liter/min, sheath gas flow 11 liter/min, capillary voltage 3,500 V, fragmentor voltage 170 V, dwell time 5 ms, cell accelerator voltage 7 V, and collision energy 28 V. Quantification data were extracted using MassHunter Quantitative Analysis (QQQ) software and manually curated to ensure correct peak integration. Areas under the curve for the extracted ion chromatogram peaks for each relevant multiple reaction monitoring transition and lipid species were isotope corrected using an in-house R script (Gao et al., 2021), and then the lipid species intensities were normalized to internal standards intensity and protein content. Individual PC species values were summed up to obtain a measure of total PC content and normalized to intensities in *Tardbp*$^{fl/fl}$ samples.

Statistical analysis

We followed the "SuperPlots" guideline (Lord et al., 2020) to show the reproducibility and variability of the experiments. All experiments using mice and cells, including immunoblotting, IF, RNA-FISH, and RNA-FISH/IF, are representative of at least three independent experiments. GraphPad and R package were used for statistical analysis. ImageJ and Imaris software were used for image analysis. Statistical tests and parameter and quantification details, including *n*, SD/SEM, and P value, are reported in the corresponding figure legends and methods. The followings are denoted for P value: #, $P < 0.10$; *, $P < 0.05$; **, $P < 0.01$; ***, $P < 0.001$; and ****, $P < 0.0001$. Data distribution was assumed to be normal, but this was not formally tested.

Mouse tissue protein extraction and protein quantification

Spinal cords were harvested and snap-frozen in liquid nitrogen before protein extraction. RIPA buffer containing 15 mM NaCl, 1% Triton X-100, 0.5% sodium deoxycholate, 0.1% SDS, and 50 mM Tris, pH 8.0, was prepared, and protease inhibitors (Thermo Fisher Scientific; 88266) were added before use. Tissues were homogenized in RIPA buffer and incubated at 4°C for 2 h with gentle agitation. After incubation, lysed samples were centrifuged at 4°C for 30 min at 20,000 ×*g* using a desktop centrifuge, and the supernatants were collected for BCA protein concentration measurement (Thermo Fisher Scientific; 23225).

Generation of human spinal organoids

Human iPSCs (hiPSCs) were cultured feeder-free on Matrigel-coated plates in MACS iPS-Brew media (Miltenyi Biotec). Routine passaging using ReLeSR (Stem Cell Technologies) was performed once every 6–7 d. Pluripotent stem cells were differentiated toward the spinal motor neuron fate following established protocols (Hor et al., 2018). Briefly, hiPSC cells were dissociated into single cells with Accutase before seeding at 30,000 cells per well in a 96-well low-attachment plate. The hiPSCs were then first neuralized by activating Wnt pathways with CHIR99021 treatment (Miltenyi Biotec; 4.25 µM) while blocking bone morphogenic protein signaling by LDN-193189

treatment (Miltenyi Biotec; 0.5 µM) at the same time. Retinoic acid (Sigma-Aldrich) was added at day 3 to the culture together with CHIR99021 and LDN-193189. The embryoid bodies were then encapsulated in 15 µl Matrigel droplets at day 10 and cultured in retinoic acid (1 µM) and purmorphamine (Miltenyi Biotec; 1 µM) to caudalize and ventralize the cultures, respectively. At day 14, encapsulated embryoid bodies were then transferred to spinner flask. Neurotrophic factors, BDNF (Miltenyi Biotec; 10 ng/ml) and GDNF (Miltenyi Biotec; 10 ng/ml), and ascorbic acid (Sigma-Aldrich; 200 µM) were added to the spinner flask at day 18 to promote organoid maturation. Organoids can be maintained for at least 120 d. N2B27 medium (50% DMEM/F12, 50% Neurobasal, 1% L-Glutamax, and 1% MEM non-essential amino acids supplemented with 1% N2 supplement and 2% B27 supplement) was used throughout the spinal organoid differentiation.

IF and confocal imaging analyses of FTLD-TDP patients

Five cases of FTLD-TDP type B were selected from the Center for Neurodegenerative Disease Research Brain Bank at the University of Pennsylvania (Toledo et al., 2014). Double IF was performed on 6-µm formalin-fixed, paraffin-embedded tissue sections from the middle frontal neocortex. After deparaffinization and rehydration, microwave antigen retrieval in citric acid–based antigen unmasking solution (Vector Laboratories) was performed on the tissues. Sections were washed in 0.1 M Tris buffer and blocked in 2% FBS in 0.1 M Tris buffer. Sections were then incubated with primary antibodies (TDP-43, Proteintech, mouse monoclonal, clone 6H6E12, 1:30,000; LDLR, Novus, rabbit polyclonal, NBP1-06709, 1:1,000; HMGCR, Thermo Fisher Scientific, rabbit polyclonal, cat #PA5-37367, 1:250; and HMGCS1, Proteintech, rabbit polyclonal, 17643-1-AP, 1:250) overnight at 4°C in a humidified chamber. Sections were washed in 0.1 M Tris buffer, blocked in 2% FBS in 0.1 M Tris buffer, and incubated with species-specific antibodies for 1–2 h at RT (Molecular Probes; Alexa Fluor 488–conjugated goat anti-mouse IgG; Alexa Fluor 647–conjugated goat anti-rabbit IgG). DAPI counterstain (Thermo Fisher Scientific; 300 µM) was used to visualize nuclei. Sections were washed and then mounted in Prolong Glass Antifade Mountant (Thermo Fisher Scientific). Z-stack confocal images were obtained using a Leica TCS SPE laser scanning confocal microscope with a 63× objective (NA 1.30) using the 405-nm, 488-nm, 561-nm, and 635-nm lasers to visualize DAPI, Alexa Fluor 488, autofluorescence, and Alexa Fluor 647, respectively. Photos were processed using Leica AF and Adobe Photoshop software.

Online supplemental material

Fig. S1 shows distinct expression profiles in the 21-d-old spinal cord tissues of *Cnp*-Cre;*Tardbp*$^{fl/fl}$ mice. Fig. S2 shows characterization of gene expression involved in lipid metabolism in oligodendroglial TDP-43 deletion mice. Fig. S3 shows reduced SREBF2 and its downstream targets in the TDP-deleted oligodendrocytes. Fig. S4 shows validation of SREBF2, LDLR, HMGCS1, and HMGCR antibodies. Fig. S5 shows characterization of mRNA levels and mRNA stability for SREBF2, HMGCR, and LDLR and lipid droplets in MO3.13 cells with TDP-43 or SREBF2 knockdown. Video 1 shows 3D reconstruction of SREBF2 and LDLR-FISH signals in oligodendrocyte. Table S1 shows sequences of PCR primers used in this study. Table S2 shows primary antibodies used in this study. Table S3 shows secondary antibodies used in this study. Table S4 shows sequences of siRNAs used in this study.

Data availability

All data are available in the main text or the supplementary materials. Sequencing data have been deposited in GEO under accession no. GSE133047.

Acknowledgments

S.-C. Ling dedicates this work to the memory of Sheue-Houy Tyan.

The authors thank Dr. David Silver and Dr. Jonah Chan for helpful comments and discussion, Dr. Edward Koo for sharing the confocal microscope, Dr. Mahmoud Pouladi (National University of Singapore, Singapore) for sharing the MO3.13 cell line, Dr. Feng Jia and Jack Wong for technical assistance, Dr. Wenhao Jin and Dr. Gene Yeo for the initial analysis on the RNA-seq data, Dr. Madushani Herath and Dr. Elisa Hill for developing and sharing the 3D-FISH quantification methods using Imaris software, and Eddy Leman and Emma Sanford for the editing of the manuscript.

The study was supported by grants to S.-C. Ling from the Swee Liew-Wadsworth Endowment Fund, National University of Singapore, National Medical Research Council (NMRC/OFIRG/0001/2016 and NMRC/OFIRG/0042/2017), and Ministry of Education - Singapore (MOE2016-T2-1-024); to M.R. Wenk, A. Cazenave-Gassiot, J.C. Foo, and S. Muralidharan from the National University of Singapore via the Life Sciences Institute and A*STAR (IAF-ICP I1901E0040), and to E.B. Lee from R01 NS095793, P30 AG072979, and P01 AG066597. A.T. Nguyen is supported by training grant T32 AG000255.

The authors declare no competing financial interests.

Author contributions: W.Y. Ho and S.-C. Ling conceived and coordinated the study. W.Y. Ho, J.C. Chang, K. Lim, G. Tucker-Kellogg, and S.-C. Ling wrote the paper. W.Y. Ho and S.-C. Ling conducted the animal and cell culture experiments. W.Y. Ho and S.J.M. Ong conducted IF-FISH experiments. W.Y. Ho and J.C. Chang conducted MO3.13 cell line experiments. K. Lim, I. Agrawal, and G. Tucker-Kellogg performed the bioinformatics analysis. J.H. Hor and S.Y. Ng generated human spinal organoids. A.T. Nguyen, A. Viera-Ortiz, O.A. Arogundade, M.J. Rodriguez, S.M. Lim, S.H. Kim, E.B. Lee, and J. Ravits conducted the post-mortem human tissue experiments. A. Cazenave-Gassiot, J.C. Foo, S. Muralidharan, and M.R. Wenk conducted the mass spectrometry analysis. W.Y. Ho and S. Hoon conducted RNA-seq experiments.

Submitted: 31 October 2019
Revised: 16 December 2020
Accepted: 28 May 2021

References

Abdel-Khalik, J., E. Yutuc, P.J. Crick, J.-A. Gustafsson, M. Warner, G. Roman, K. Talbot, E. Gray, W.J. Griffiths, M.R. Turner, and Y. Wang. 2017. Defective cholesterol metabolism in amyotrophic lateral sclerosis. *J. Lipid Res.* 58:267–278. https://doi.org/10.1194/jlr.P071639

Aoki, N., M.E. Murray, K. Ogaki, S. Fujioka, N.J. Rutherford, R. Rademakers, O.A. Ross, and D.W. Dickson. 2015. Hippocampal sclerosis in Lewy body

disease is a TDP-43 proteinopathy similar to FTLD-TDP Type A. *Acta Neuropathol.* 129:53–64. https://doi.org/10.1007/s00401-014-1358-z

Bandres Ciga, S., A.J. Noyce, G. Hemani, A. Nicolas, A. Calvo, G. Mora, P.J. Tienari, D.J. Stone, M.A. Nalls, A.B. Singleton, et al. International ALS Genomics Consortium. 2019. Shared polygenic risk and causal inferences in amyotrophic lateral sclerosis. *Ann. Neurol.* 85:470–481. https://doi.org/10.1002/ana.25431

Berghoff, S.A., N. Gerndt, J. Winchenbach, S.K. Stumpf, L. Hosang, F. Odoardi, T. Ruhwedel, C. Böhler, B. Barrette, R. Stassart, et al. 2017. Dietary cholesterol promotes repair of demyelinated lesions in the adult brain. *Nat. Commun.* 8:14241. https://doi.org/10.1038/ncomms14241

Bin, J.M., S.N. Harris, and T.E. Kennedy. 2016. The oligodendrocyte-specific antibody 'CC1' binds Quaking 7. *J. Neurochem.* 139:181–186. https://doi.org/10.1111/jnc.13745

Björkhem, I., V. Leoni, and S. Meaney. 2010. Genetic connections between neurological disorders and cholesterol metabolism. *J. Lipid Res.* 51:2489–2503. https://doi.org/10.1194/jlr.R006338

Bligh, E.G., and W.J. Dyer. 1959. A rapid method of total lipid extraction and purification. *Can. J. Biochem. Physiol.* 37:911–917. https://doi.org/10.1139/o59-099

Brown, M.S., and J.L. Goldstein. 2009. Cholesterol feedback: from Schoenheimer's bottle to Scap's MELADL. *J. Lipid Res.* 50(Suppl):S15–S27. https://doi.org/10.1194/jlr.R800054-JLR200

Brown, M.S., A. Radhakrishnan, and J.L. Goldstein. 2018. Retrospective on Cholesterol Homeostasis: The Central Role of Scap. *Annu. Rev. Biochem.* 87:783–807. https://doi.org/10.1146/annurev-biochem-062917-011852

Camargo, N., J.F. Brouwers, M. Loos, D.H. Gutmann, A.B. Smit, and M.H.G. Verheijen. 2012. High-fat diet ameliorates neurological deficits caused by defective astrocyte lipid metabolism. *FASEB J.* 26:4302–4315. https://doi.org/10.1096/fj.12-205807

Camargo, N., A. Goudriaan, A.F. van Deijk, W.M. Otte, J.F. Brouwers, H. Lodder, D.H. Gutmann, K.-A. Nave, R.M. Dijkhuizen, H.D. Mansvelder, et al. 2017. Oligodendroglial myelination requires astrocyte-derived lipids. *PLoS Biol.* 15:e1002605–e1002624. https://doi.org/10.1371/journal.pbio.1002605

Cantuti-Castelvetri, L., D. Fitzner, M. Bosch-Queralt, M.-T. Weil, M. Su, P. Sen, T. Ruhwedel, M. Mitkovski, G. Trendelenburg, D. Lütjohann, et al. 2018. Defective cholesterol clearance limits remyelination in the aged central nervous system. *Science.* 359:684–688. https://doi.org/10.1126/science.aan4183

Chang, J.-C., D.J. Hazelett, J.A. Stewart, and D.B. Morton. 2014. Motor neuron expression of the voltage-gated calcium channel cacophony restores locomotion defects in a Drosophila, TDP-43 loss of function model of ALS. *Brain Res.* 1584:39–51. https://doi.org/10.1016/j.brainres.2013.11.019

Cheng, C., P. Ru, F. Geng, J. Liu, J.Y. Yoo, X. Wu, X. Cheng, V. Euthine, P. Hu, J.Y. Guo, et al. 2015. Glucose-Mediated N-glycosylation of SCAP Is Essential for SREBP-1 Activation and Tumor Growth. *Cancer Cell.* 28:569–581. https://doi.org/10.1016/j.ccell.2015.09.021

Chiò, A., M. Brunetti, M. Barberis, B. Iazzolino, A. Montuschi, A. Ilardi, S. Cammarosano, A. Canosa, C. Moglia, and A. Calvo. 2016. The Role of APOE in the Occurrence of Frontotemporal Dementia in Amyotrophic Lateral Sclerosis. *JAMA Neurol.* 73:425–430. https://doi.org/10.1001/jamaneurol.2015.4773

Dietschy, J.M., and S.D. Turley. 2004. Thematic review series: brain Lipids. Cholesterol metabolism in the central nervous system during early development and in the mature animal. *J. Lipid Res.* 45:1375–1397. https://doi.org/10.1194/jlr.R400004-JLR200

Engelking, L.J., M.J. Cantoria, Y. Xu, and G. Liang. 2018. Developmental and extrahepatic physiological functions of SREBP pathway genes in mice. *Semin. Cell Dev. Biol.* 81:98–109. https://doi.org/10.1016/j.semcdb.2017.07.011

Fiesel, F.C., S.S. Weber, J. Supper, A. Zell, and P.J. Kahle. 2012. TDP-43 regulates global translational yield by splicing of exon junction complex component SKAR. *Nucleic Acids Res.* 40:2668–2682. https://doi.org/10.1093/nar/gkr1082

Gao, L., S. Ji, B. Burla, M.R. Wenk, F. Torta, and A. Cazenave-Gassiot. 2021. LICAR: An Application for Isotopic Correction of Targeted Lipidomic Data Acquired with Class-Based Chromatographic Separations Using Multiple Reaction Monitoring. *Anal. Chem.* 93:3163–3171. https://doi.org/10.1021/acs.analchem.0c04565

Garbuzova-Davis, S., D.G. Hernandez-Ontiveros, M.C.O. Rodrigues, E. Haller, A. Frisina-Deyo, S. Mirtyl, S. Sallot, S. Saporta, C.V. Borlongan, and P.R. Sanberg. 2012. Impaired blood-brain/spinal cord barrier in ALS patients. *Brain Res.* 1469:114–128. https://doi.org/10.1016/j.brainres.2012.05.056

Gibson, E.M., D. Purger, C.W. Mount, A.K. Goldstein, G.L. Lin, L.S. Wood, I. Inema, S.E. Miller, G. Bieri, J.B. Zuchero, et al. 2014. Neuronal activity promotes oligodendrogenesis and adaptive myelination in the mammalian brain. *Science.* 344:1252304. https://doi.org/10.1126/science.1252304

Goldstein, J.L., and M.S. Brown. 2015. A century of cholesterol and coronaries: from plaques to genes to statins. *Cell.* 161:161–172. https://doi.org/10.1016/j.cell.2015.01.036

Golomb, B.A., A. Verden, A.K. Messner, H.J. Koslik, and K.B. Hoffman. 2018. Amyotrophic Lateral Sclerosis Associated with Statin Use: A Disproportionality Analysis of the FDA's Adverse Event Reporting System. *Drug Saf.* 41:403–413. https://doi.org/10.1007/s40264-017-0620-4

Hill, R.A., A.M. Li, and J. Grutzendler. 2018. Lifelong cortical myelin plasticity and age-related degeneration in the live mammalian brain. *Nat. Neurosci.* 21:683–695. https://doi.org/10.1038/s41593-018-0120-6

Hor, J.H., E.S.-Y. Soh, L.Y. Tan, V.J.W. Lim, M.M. Santosa, B.X. Winanto, B.X. Ho, Y. Fan, B.S. Soh, and S.Y. Ng. 2018. Cell cycle inhibitors protect motor neurons in an organoid model of Spinal Muscular Atrophy. *Cell Death Dis.* 9:1100. https://doi.org/10.1038/s41419-018-1081-0

Horton, J.D., J.L. Goldstein, and M.S. Brown. 2002. SREBPs: activators of the complete program of cholesterol and fatty acid synthesis in the liver. *J. Clin. Invest.* 109:1125–1131. https://doi.org/10.1172/JCI0215593

Horton, J.D., N.A. Shah, J.A. Warrington, N.N. Anderson, S.W. Park, M.S. Brown, and J.L. Goldstein. 2003. Combined analysis of oligonucleotide microarray data from transgenic and knockout mice identifies direct SREBP target genes. *Proc. Natl. Acad. Sci. USA.* 100:12027–12032. https://doi.org/10.1073/pnas.1534923100

Josephs, K.A., M.E. Murray, J.L. Whitwell, J.E. Parisi, L. Petrucelli, C.R. Jack, R.C. Petersen, and D.W. Dickson. 2014. Staging TDP-43 pathology in Alzheimer's disease. *Acta Neuropathol.* 127:441–450. https://doi.org/10.1007/s00401-013-1211-9

Jurevics, H., and P. Morell. 1995. Cholesterol for synthesis of myelin is made locally, not imported into brain. *J. Neurochem.* 64:895–901. https://doi.org/10.1046/j.1471-4159.1995.64020895.x

Lagier-Tourenne, C., M. Polymenidou, and D.W. Cleveland. 2010. TDP-43 and FUS/TLS: emerging roles in RNA processing and neurodegeneration. *Hum. Mol. Genet.* 19(R1):R46–R64. https://doi.org/10.1093/hmg/ddq137

Lee, E.B., V.M.-Y. Lee, and J.Q. Trojanowski. 2011. Gains or losses: molecular mechanisms of TDP43-mediated neurodegeneration. *Nat. Rev. Neurosci.* 13:38–50. https://doi.org/10.1038/nrn3121

Lee, Y., B.M. Morrison, Y. Li, S. Lengacher, M.H. Farah, P.N. Hoffman, Y. Liu, A. Tsingalia, L. Jin, P.-W. Zhang, et al. 2012. Oligodendroglia metabolically support axons and contribute to neurodegeneration. *Nature.* 487:443–448. https://doi.org/10.1038/nature11314

Lee, E.B., S. Porta, G. Michael Baer, Y. Xu, E. Suh, L.K. Kwong, L. Elman, M. Grossman, V.M.-Y. Lee, D.J. Irwin, et al. 2017. Expansion of the classification of FTLD-TDP: distinct pathology associated with rapidly progressive frontotemporal degeneration. *Acta Neuropathol.* 134:65–78. https://doi.org/10.1007/s00401-017-1679-9

Ling, S.-C., C.P. Albuquerque, J.S. Han, C. Lagier-Tourenne, S. Tokunaga, H. Zhou, and D.W. Cleveland. 2010. ALS-associated mutations in TDP-43 increase its stability and promote TDP-43 complexes with FUS/TLS. *Proc. Natl. Acad. Sci. USA.* 107:13318–13323. https://doi.org/10.1073/pnas.1008227107

Ling, S.-C., M. Polymenidou, and D.W. Cleveland. 2013. Converging mechanisms in ALS and FTD: disrupted RNA and protein homeostasis. *Neuron.* 79:416–438. https://doi.org/10.1016/j.neuron.2013.07.033

Listenberger, L.L., and D.A. Brown. 2007. Fluorescent Detection of Lipid Droplets and Associated Proteins. *Curr. Protoc. Cell Biol.* 35:24.2.1-24.2.11. doi:. https://doi.org/10.1002/0471143030.cb2402s35

Lord, S.J., K.B. Velle, R.D. Mullins, and L.K. Fritz-Laylin. 2020. SuperPlots: Communicating reproducibility and variability in cell biology. *J. Cell Biol.* 219:e202001064. https://doi.org/10.1083/jcb.202001064

Majumder, P., J.-F. Chu, B. Chatterjee, K.B.S. Swamy, and C.J. Shen. 2016. Co-regulation of mRNA translation by TDP-43 and Fragile X Syndrome protein FMRP. *Acta Neuropathol.* 132:721–738. https://doi.org/10.1007/s00401-016-1603-8

Mariosa, D., N. Hammar, H. Malmström, C. Ingre, I. Jungner, W. Ye, F. Fang, and G. Walldius. 2017. Blood biomarkers of carbohydrate, lipid, and apolipoprotein metabolisms and risk of amyotrophic lateral sclerosis: A more than 20-year follow-up of the Swedish AMORIS cohort. *Ann. Neurol.* 81:718–728. https://doi.org/10.1002/ana.24936

Martín, M.G., F. Pfrieger, and C.G. Dotti. 2014. Cholesterol in brain disease: sometimes determinant and frequently implicated. *EMBO Rep.* 15:1036–1052. https://doi.org/10.15252/embr.201439225

McKenzie, I.A., D. Ohayon, H. Li, J.P. de Faria, B. Emery, K. Tohyama, and W.D. Richardson. 2014. Motor skill learning requires active central myelination. *Science.* 346:318–322. https://doi.org/10.1126/science.1254960

Nagano, S., J. Jinno, R.F. Abdelhamid, Y. Jin, M. Shibata, S. Watanabe, S. Hirokawa, M. Nishizawa, K. Sakimura, O. Onodera, et al. 2020. TDP-43 transports ribosomal protein mRNA to regulate axonal local translation in neuronal axons. *Acta Neuropathol.* 140:695–713. https://doi.org/10.1007/s00401-020-02205-y

Nathans, D. 1964. PUROMYCIN INHIBITION OF PROTEIN SYNTHESIS: INCORPORATION OF PUROMYCIN INTO PEPTIDE CHAINS. *Proc. Natl. Acad. Sci. USA.* 51:585–592. https://doi.org/10.1073/pnas.51.4.585

Nave, K.-A., and H.B. Werner. 2014. Myelination of the nervous system: mechanisms and functions. *Annu. Rev. Cell Dev. Biol.* 30:503–533. https://doi.org/10.1146/annurev-cellbio-100913-013101

Neumann, M., D.M. Sampathu, L.K. Kwong, A.C. Truax, M.C. Micsenyi, T.T. Chou, J. Bruce, T. Schuck, M. Grossman, C.M. Clark, et al. 2006. Ubiquitinated TDP-43 in frontotemporal lobar degeneration and amyotrophic lateral sclerosis. *Science.* 314:130–133. https://doi.org/10.1126/science.1134108

Peng, A.Y.T., I. Agrawal, W.Y. Ho, Y.-C. Yen, A.J. Pinter, J. Liu, Q.X.C. Phua, K.B. Koh, J.-C. Chang, E. Sanford, et al. 2020. Loss of TDP-43 in astrocytes leads to motor deficits by triggering A1-like reactive phenotype and triglial dysfunction. *Proc. Natl. Acad. Sci. USA.* 117:29101–29112. https://doi.org/10.1073/pnas.2007806117

Pfeiffer, S.E., A.E. Warrington, and R. Bansal. 1993. The oligodendrocyte and its many cellular processes. *Trends Cell Biol.* 3:191–197. https://doi.org/10.1016/0962-8924(93)90213-K

Platt, F.M., C. Wassif, A. Colaco, A. Dardis, E. Lloyd-Evans, B. Bembi, and F.D. Porter. 2014. Disorders of cholesterol metabolism and their unanticipated convergent mechanisms of disease. *Annu. Rev. Genomics Hum. Genet.* 15:173–194. https://doi.org/10.1146/annurev-genom-091212-153412

Polymenidou, M., C. Lagier-Tourenne, K.R. Hutt, S.C. Huelga, J. Moran, T.Y. Liang, S.-C. Ling, E. Sun, E. Wancewicz, C. Mazur, et al. 2011. Long pre-mRNA depletion and RNA missplicing contribute to neuronal vulnerability from loss of TDP-43. *Nat. Neurosci.* 14:459–468. https://doi.org/10.1038/nn.2779

Quan, G., C. Xie, J.M. Dietschy, and S.D. Turley. 2003. Ontogenesis and regulation of cholesterol metabolism in the central nervous system of the mouse. *Brain Res. Dev. Brain Res.* 146:87–98. https://doi.org/10.1016/j.devbrainres.2003.09.015

Ratnadiwakara, M., S.K. Archer, C.I. Dent, I. Ruiz De Los Mozos, T.H. Beilharz, A.S. Knaupp, C.M. Nefzger, J.M. Polo, and M.-L. Anko. 2018. SRSF3 promotes pluripotency through *Nanog* mRNA export and coordination of the pluripotency gene expression program. *eLife.* 7:e37419. https://doi.org/10.7554/eLife.37419

Ryan, A.K., K. Bartlett, P. Clayton, S. Eaton, L. Mills, D. Donnai, R.M. Winter, and J. Burn. 1998. Smith-Lemli-Opitz syndrome: a variable clinical and biochemical phenotype. *J. Med. Genet.* 35:558–565. https://doi.org/10.1136/jmg.35.7.558

Saher, G., and S.K. Stumpf. 2015. Cholesterol in myelin biogenesis and hypomyelinating disorders. *Biochim. Biophys. Acta.* 1851:1083–1094. doi:. https://doi.org/10.1016/j.bbalip.2015.02.010

Saher, G., B. Brügger, C. Lappe-Siefke, W. Möbius, R. Tozawa, M.C. Wehr, F. Wieland, S. Ishibashi, and K.-A. Nave. 2005. High cholesterol level is essential for myelin membrane growth. *Nat. Neurosci.* 8:468–475. https://doi.org/10.1038/nn1426

Saher, G., F. Rudolphi, K. Corthals, T. Ruhwedel, K.-F. Schmidt, S. Löwel, P. Dibaj, B. Barrette, W. Möbius, and K.-A. Nave. 2012. Therapy of Pelizaeus-Merzbacher disease in mice by feeding a cholesterol-enriched diet. *Nat. Med.* 18:1130–1135. https://doi.org/10.1038/nm.2833

Schmidt, E.K., G. Clavarino, M. Ceppi, and P. Pierre. 2009. SUnSET, a nonradioactive method to monitor protein synthesis. *Nat. Methods.* 6:275–277. https://doi.org/10.1038/nmeth.1314

Sharpe, L.J., E.C.L. Cook, N. Zelcer, and A.J. Brown. 2014. The UPS and downs of cholesterol homeostasis. *Trends Biochem. Sci.* 39:527–535. https://doi.org/10.1016/j.tibs.2014.08.008

Singh, J., and R.A. Padgett. 2009. Rates of in situ transcription and splicing in large human genes. *Nat. Struct. Mol. Biol.* 16:1128–1133. https://doi.org/10.1038/nsmb.1666

Son, H.-H., J.-Y. Moon, H.S. Seo, H.H. Kim, B.C. Chung, and M.H. Choi. 2014. High-temperature GC-MS-based serum cholesterol signatures may reveal sex differences in vasospastic angina. *J. Lipid Res.* 55:155–162. https://doi.org/10.1194/jlr.D040790

Tan, R.H., Y.D. Ke, L.M. Ittner, and G.M. Halliday. 2017. ALS/FTLD: experimental models and reality. *Acta Neuropathol.* 133:177–196. https://doi.org/10.1007/s00401-016-1666-6

Toledo, J.B., V.M. Van Deerlin, E.B. Lee, E. Suh, Y. Baek, J.L. Robinson, S.X. Xie, J. McBride, E.M. Wood, T. Schuck, et al. 2014. A platform for discovery: The University of Pennsylvania Integrated Neurodegenerative Disease Biobank. *Alzheimers Dement.* 10:477–484.e1. https://doi.org/10.1016/j.jalz.2013.06.003

van der Kant, R., V.F. Langness, C.M. Herrera, D.A. Williams, L.K. Fong, Y. Leestemaker, E. Steenvoorden, K.D. Rynearson, J.F. Brouwers, J.B. Helms, et al. 2019. Cholesterol Metabolism Is a Druggable Axis that Independently Regulates Tau and Amyloid-β in iPSC-Derived Alzheimer's Disease Neurons. *Cell Stem Cell.* 24:363–375.e9. https://doi.org/10.1016/j.stem.2018.12.013

Wake, H., P.R. Lee, and R.D. Fields. 2011. Control of local protein synthesis and initial events in myelination by action potentials. *Science.* 333:1647–1651. https://doi.org/10.1126/science.1206998

Wang, I.-F., L.-S. Wu, H.-Y. Chang, and C.-K.J. Shen. 2008. TDP-43, the signature protein of FTLD-U, is a neuronal activity-responsive factor. *J. Neurochem.* 105:797–806. https://doi.org/10.1111/j.1471-4159.2007.05190.x

Wang, J., W.Y. Ho, K. Lim, J. Feng, G. Tucker-Kellogg, K.-A. Nave, and S.-C. Ling. 2018. Cell-autonomous requirement of TDP-43, an ALS/FTD signature protein, for oligodendrocyte survival and myelination. *Proc. Natl. Acad. Sci. USA.* 115:E10941–E10950. https://doi.org/10.1073/pnas.1809821115

Winkler, E.A., J.D. Sengillo, J.S. Sullivan, J.S. Henkel, S.H. Appel, and B.V. Zlokovic. 2013. Blood-spinal cord barrier breakdown and pericyte reductions in amyotrophic lateral sclerosis. *Acta Neuropathol.* 125:111–120. https://doi.org/10.1007/s00401-012-1039-8

Yang, H.-S., L. Yu, C.C. White, L.B. Chibnik, J.P. Chhatwal, R.A. Sperling, D.A. Bennett, J.A. Schneider, and P.L. De Jager. 2018. Evaluation of TDP-43 proteinopathy and hippocampal sclerosis in relation to APOE ε4 haplotype status: a community-based cohort study. *Lancet Neurol.* 17:773–781. https://doi.org/10.1016/S1474-4422(18)30251-5

Yang, Y-C.T., C. Di, B. Hu, M. Zhou, Y. Liu, N. Song, Y. Li, J. Umetsu, and Z. Lu. 2015. CLIPdb: a CLIP-seq database for protein-RNA interactions. *BMC Genomics.* 16:51. https://doi.org/10.1186/s12864-015-1273-2

Zeng, P., and X. Zhou. 2019. Causal effects of blood lipids on amyotrophic lateral sclerosis: a Mendelian randomization study. *Hum. Mol. Genet.* 28:688–697. https://doi.org/10.1093/hmg/ddy384

Zhao, S., X. Hu, J. Park, Y. Zhu, Q. Zhu, H. Li, C. Luo, R. Han, N. Cooper, and M. Qiu. 2007. Selective expression of LDLR and VLDLR in myelinating oligodendrocytes. *Dev. Dyn.* 236:2708–2712. https://doi.org/10.1002/dvdy.21283

JCB

Supplemental material

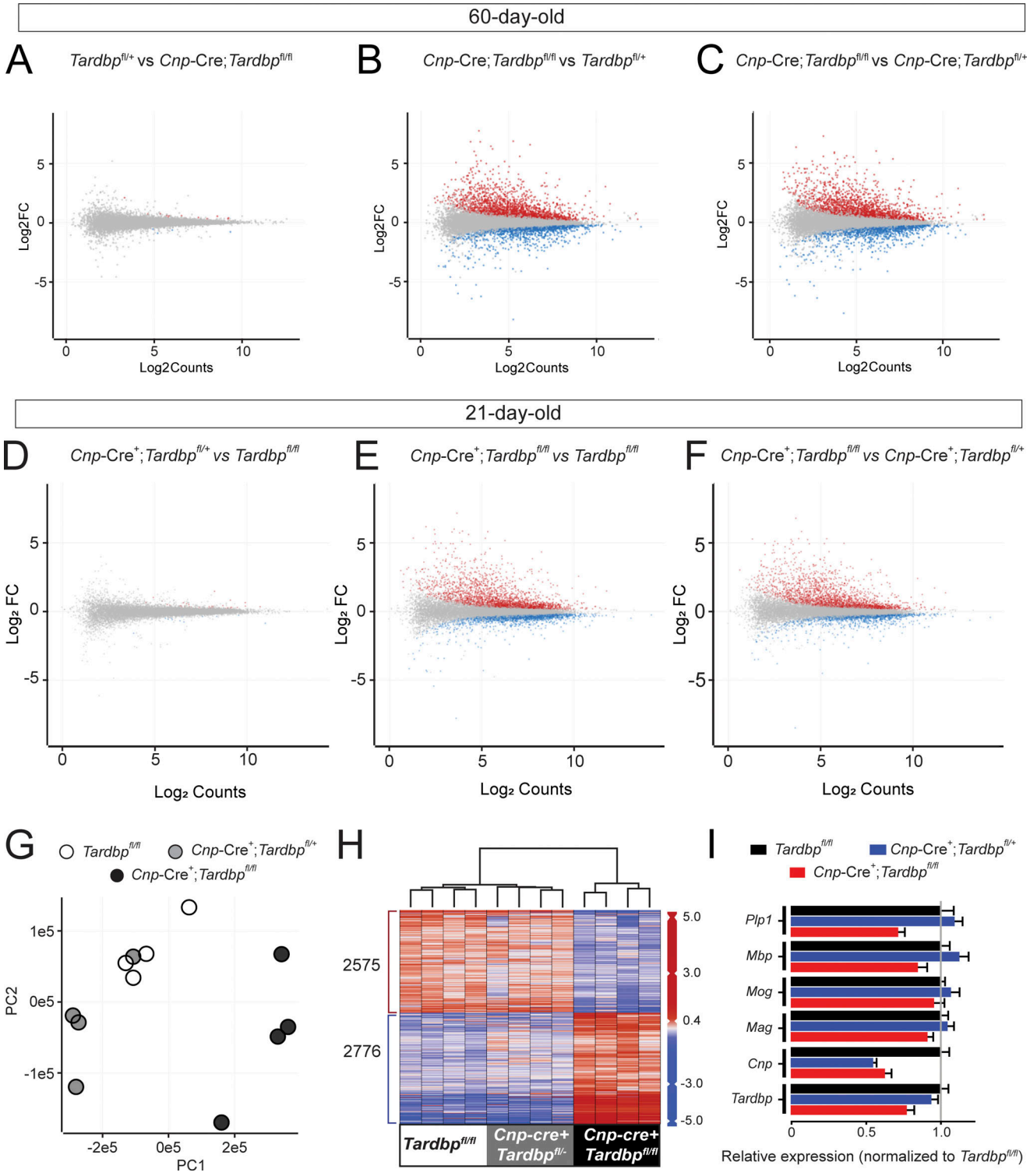

Figure S1. **Distinct expression profiles in the 21-d-old spinal cord tissues of *Cnp*-Cre;*Tardbp*$^{fl/fl}$ mice. (A–C)** MA plots of pairwise contrasts between *Tardbp*$^{fl/fl}$ (ctrl), *Cnp*-Cre;*Tardbp*$^{fl/+}$ (cHet), and *Cnp*-Cre;*Tardbp*$^{fl/fl}$ (cKO) transcriptomes (P60) reveal patterns of differential expression (FDR-corrected P value <0.1; red: up-regulated; blue: down-regulated) between *Cnp*-Cre;*Tardbp*$^{fl/fl}$ and *Tardbp*$^{fl/fl}$/*Cnp*-Cre;*Tardbp*$^{fl/+}$ conditions, but not between *Tardbp*$^{fl/fl}$ and *Cnp*-Cre;*Tardbp*$^{fl/+}$ mice. **(D–F)** MA plots of pairwise contrasts between *Tardbp*$^{fl/fl}$ (ctrl), *Cnp*-Cre;*Tardbp*$^{fl/+}$ (cHet), and *Cnp*-Cre;*Tardbp*$^{fl/fl}$ (cKO) transcriptomes (P21) reveal patterns of differential expression (FDR-corrected P value <0.1; red: up-regulated; blue: down-regulated) between *Cnp*-Cre;*Tardbp*$^{fl/fl}$ and *Tardbp*$^{fl/fl}$/*Cnp*-Cre;*Tardbp*$^{fl/+}$ conditions, but not between *Tardbp*$^{fl/fl}$ and *Cnp*-Cre;*Tardbp*$^{fl/+}$ mice. **(G)** PCA of count data across all three conditions shows a clear separation of *Cnp*-Cre;*Tardbp*$^{fl/fl}$ and *Tardbp*$^{fl/fl}$/*Cnp*-Cre;*Tardbp*$^{fl/+}$ data across the first two principal components at P21. **(H)** Hierarchical clustering of gene-centered count data cleanly categorizes the data, with *Cnp*-Cre;*Tardbp*$^{fl/fl}$ samples clustered separately from both *Tardbp*$^{fl/fl}$ and *Cnp*-Cre;*Tardbp*$^{fl/+}$ samples at P21. **(I)** Normalized expression information for myelin-related and knockout-related genes at P21. Error bars describe expression SD. cHet, conditional heterozygous knockout; cKO, conditional knockout; ctrl, control.

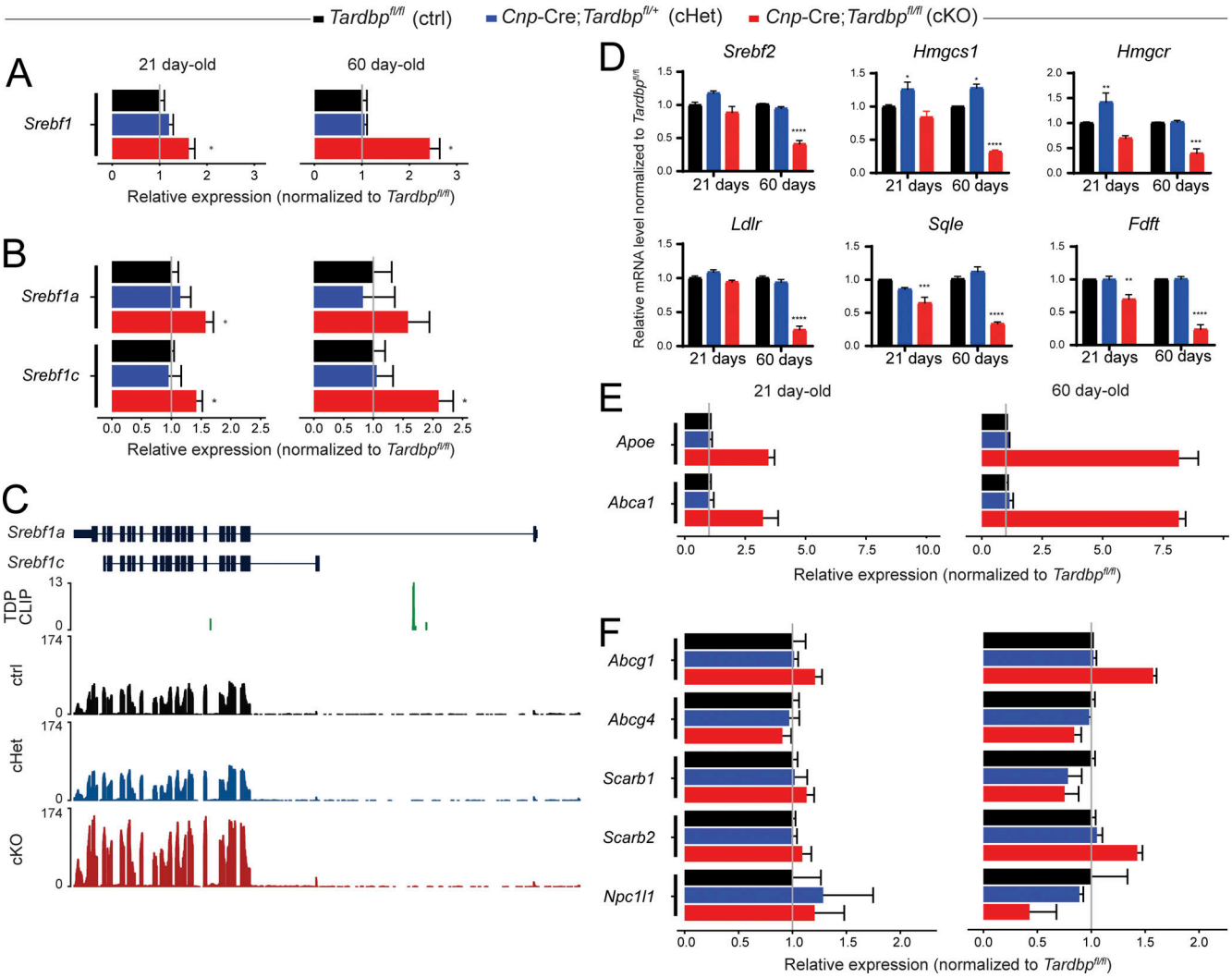

Figure S2. **Characterization of gene expression involved in lipid metabolism in oligodendroglial TDP-43 deletion mice. (A)** Normalized gene expression data for the *Srebf1* gene shows an increase in *Srebf1* levels after knockout in P21 and P60 mice. *, FDR-corrected P value <0.1 for *Cnp*-Cre^{+};*Tardbp*$^{fl/fl}$ versus *Cnp*-Cre^{+};*Tardbp*$^{fl/+}$contrast. Error bars describe expression SD. **(B)** Normalized transcript expression data for *Srebf1a* (ENSMUST00000020846.7) and *Srebf1c* (ENSMUST00000144942.1) show a significant increase in *Srebf1c* but not *Srebf1a* expression in 60-d-old mice. *, FDR-corrected P value <0.1 for *Cnp*-Cre^{+}; *Tardbp*$^{fl/fl}$ versus *Cnp*-Cre^{+};*Tardbp*$^{fl/+}$contrast. Error bars describe expression SD. **(C)** Data summary for selected *Srebf1* including Transcript structure model, CLIP-seq coverage (green), and RNA-seq coverage for *Tardbp*$^{fl/fl}$ (black), *Cnp*-Cre^{+};*Tardbp*$^{fl/+}$ (blue), and *Cnp*-Cre^{+};*Tardbp*$^{fl/fl}$ (red) conditions. **(D)** RT-qPCR conformation of RNA-seq results on cholesterol genes in *Cnp*-Cre;*Tardbp*$^{fl/fl}$ mice. mRNA levels of *Srebf-2*, *Hmgcs1*, *Hmgcr*, *Fdft1*, *Sqle*, and *Ldlr* were measured by RT-qPCR using spinal cord RNA samples from *Tardbp*$^{fl/fl}$, *Cnp*-Cre^{+};*Tardbp*$^{fl/+}$, and *Cnp*-Cre^{+};*Tardbp*$^{fl/fl}$ mice at 21- and 60-d time points. At least three animals per genotype per group were used. One-way ANOVA with Tukey's multiple comparisons test was used to evaluate statistical significance; *, P < 0.05; **, P < 0.01; ***, P < 0.001; ****, P < 0.0001. **(E and F)** Compensatory increase of genes involving in cholesterol efflux pathway. Normalized gene expression data for cholesterol efflux–associated genes show a progressive up-regulation of key efflux genes (*Apoe*, *Abca1*, and *Abcg1*) in P21 and P60 samples. *, FDR-corrected P value <0.1 for *Cnp*-Cre^{+};*Tardbp*$^{fl/fl}$ versus *Cnp*-Cre^{+};*Tardbp*$^{fl/+}$contrast. Error bars describe expression SD. cHet, conditional heterozygous knockout; cKO, conditional knockout; ctrl, control.

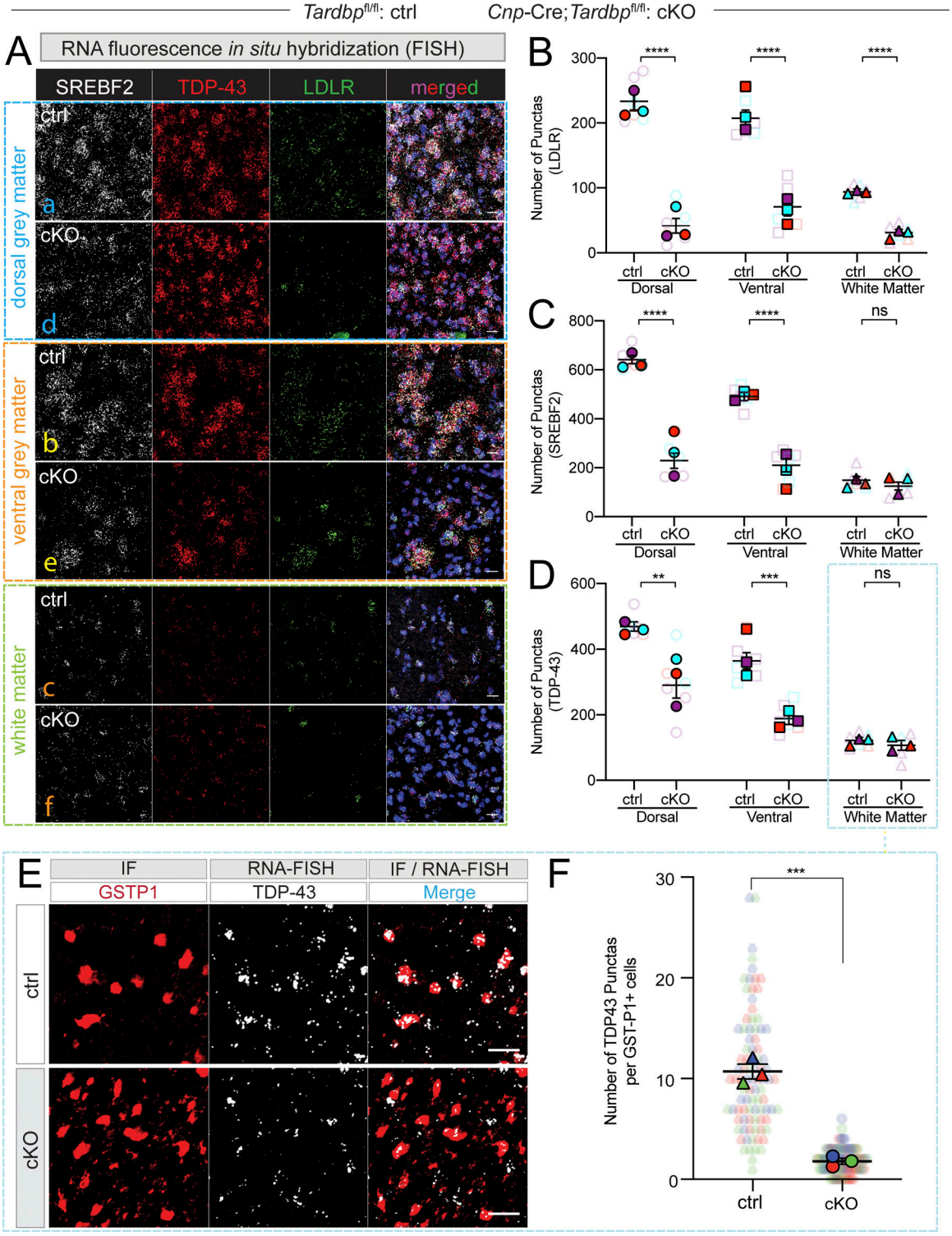

Figure S3. **Reduced SREBF2 and its downstream targets in the TDP-43-deleted oligodendrocytes. (A)** Confocal images of RNA-FISH of SREBF2, TDP-43, and LDLR assays using *Tardbp*$^{fl/fl}$ (ctrl) and *Cnp*-Cre;*Tardbp*$^{fl/fl}$ (cKO) conditions. Images shown are from dorsal gray, ventral gray, and white matter at P60. Scale bar: 20 µm. **(B–D)** Quantification of FISH signals across dorsal gray, ventral gray, and white matter for LDLR (B), SREBF2 (C), and TDP-43 (D). Puncta counts of individual oligodendrocytes (faded circle or triangle or square) and means (solid circle or triangle or square) for animal (n = 3) plotted, total mean ± SEM derived from all animals. Significance was tested using unpaired t test; **, P < 0.01; ***, P < 0.001; ****, P < 0.0001. n = 3 per genotype, at least three slices per animals were quantified. **(E)** Confocal images of RNA-FISH of TDP43 and IF of GSTP1 assays using *Tardbp*$^{fl/fl}$ (ctrl) and *Cnp*-Cre;*Tardbp*$^{fl/fl}$ (cKO) conditions. Images shown are from the white matter. Scale bar: 20 µm. **(F)** Quantification of FISH signals in white matter for TDP43 in GSTP1^{+} cells. Puncta counts of individual oligodendrocytes (faded circle or triangle) and means (solid circle or triangle) for each set of experiment (n = 3) plotted, total mean ± SEM derived from all animals. Significance was tested using unpaired t test; ***, P < 0.001. n = 3 per genotype, at least three slices per animals were quantified. cKO, conditional knockout; ctrl, control.

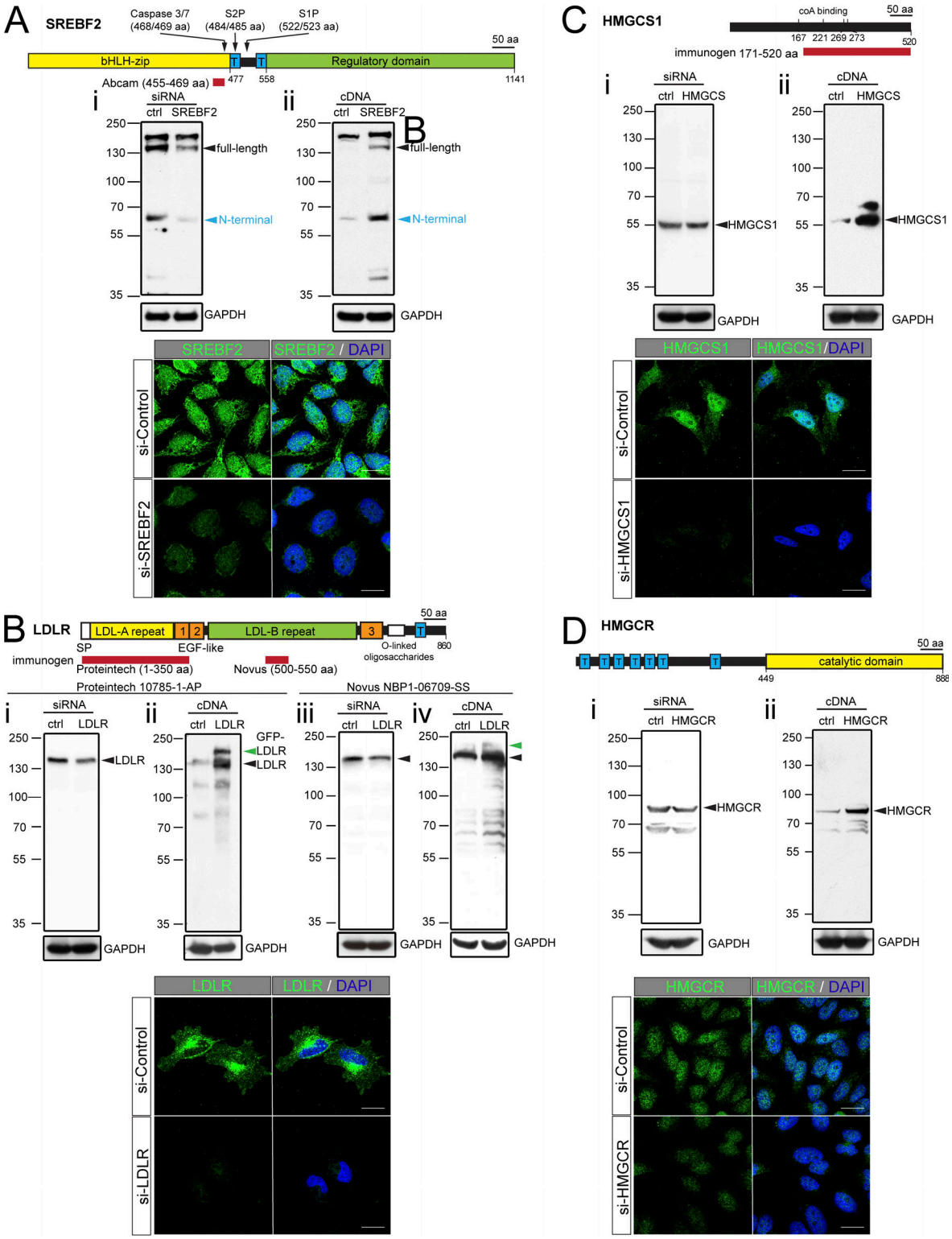

Figure S4. **Validation of SREBF2, LDLR, HMGCS1, and HMGCR antibodies. (A)** Domain organization of human SREBF2 protein. Antibody epitope is within 455–469 aa. Cell lysates from (i) siRNA-control and siRNA-SREBF2, (ii) control plasmid and full-length cDNA expressing SREBF2. Black arrow: full-length SREBF2; blue arrow: N-terminal processed transcription domain. **(B)** Domain organization of human LDLR protein. Antibodies were produced using recombinant protein within 1–350 aa (for Proteintech, 10785–1-AP) or 500–550 aa (Novus, NBP1-06709-SS) for LDLR. Cell lysates from (i and iii) siRNA-control and siRNA-LDLR, and (ii and iv) control plasmid and full-length cDNA expressing GFP-LDLR. Black arrow: endogenous LDLR; green arrow: GFP-LDLR. **(C)** Domain organization of human HMGCS1 protein. Antibody was produced using recombinant protein within 171–520 aa. Cell lysates from (i) siRNA-control and siRNA-HMGCS1, and (ii) control plasmid and full-length cDNA expressing HMGCS1. Black arrow: endogenous HMGCS1. **(D)** Domain organization of human HMGCR protein. Cell lysates from (i) siRNA-control and siRNA-HMGCR, and (ii) control plasmid and full-length cDNA expressing HMGCR. Black arrow: endogenous HMGCR. ctrl, control.

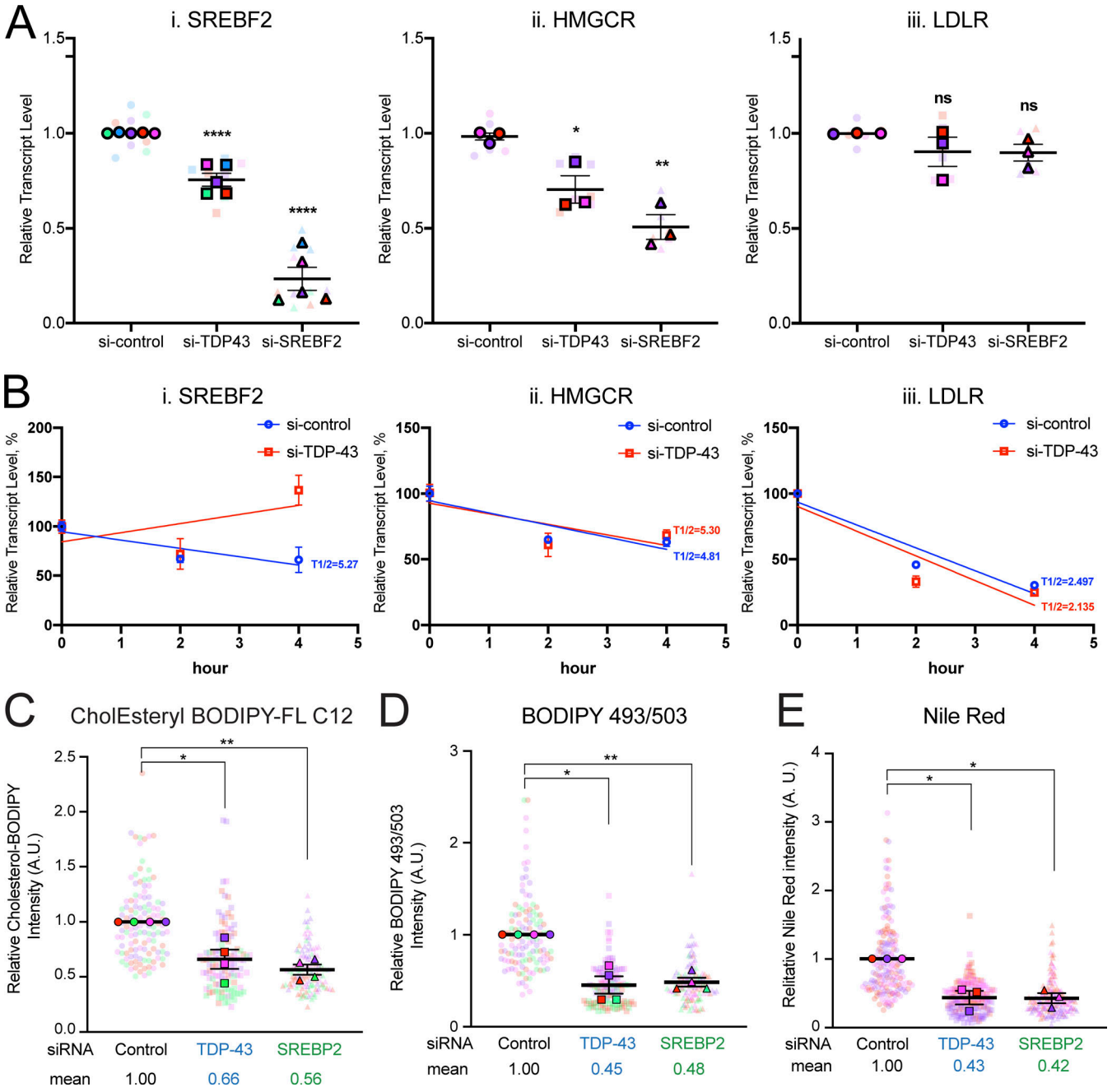

Figure S5. **Characterization of mRNA levels and mRNA stability for SREBF2, HMGCR, and LDLR, and lipid droplets in MO3.13 cells with TDP-43 or SREBF2 knockdown. (A)** RT-qPCR for (i) SREBF2, (ii) HMGCR, and (iii) LDLR in MO3.13 cells treated with siRNA-(negative) control, si-TDP-43, and si-SREBF2. The steady-state of SREBF2 and HMGCR mRNA was reduced in TDP-43 and SREBF2 knock-down conditions. Three independent experiments were performed, and three biological samples were performed per experiment. One-way ANOVA with Tukey's multiple comparisons tests was used to evaluate statistical significance: *, $P < 0.05$; **, $P < 0.01$; ****, $P < 0.0001$. **(B)** RNA half-lives for (i) SREBF2, (ii) HMGCR, and (iii) LDLR mRNAs in MO3.13 cells treated with siRNA-(negative) control and si-TDP-43. Three independent experiments were performed, and three biological samples were performed per experiment. **(C)** The relative cholesteryl-BODIPY fluorescent intensity in cells treated with control siRNA, siRNA against TDP-43, or SREBF2. *, $P < 0.05$; **, $P < 0.01$. Quantification was done from three independent experiments with >25 cells quantified per experiment. **(D)** Relative BODIPY-493/503 fluorescent intensity in cells treated with control siRNA, siRNA against TDP-43, or SREBF2. *, $P < 0.05$; **, $P < 0.01$. Quantification was done from three independent experiments with >40 cells quantified per experiment. **(E)** Relative Nile Red fluorescent intensity in cells treated with control siRNA, siRNA against TDP-43, or SREBF2. *, $P < 0.05$; **, $P < 0.01$. Quantification was done from three independent experiments with >25 cells quantified per experiment. One-way ANOVA with Tukey's multiple comparisons tests was used to evaluate statistical significance for C–E.

Video 1. **3D reconstruction of SREBF2 and LDLR-FISH signals in oligodendrocyte.** Representative oligodendrocyte from control mouse spinal cord reconstructed in 3D based on GST-P1 (red) IF signal and LDLR (green) and SREBF2 (purple) RNA-FISH signals.

Four tables are provided online as separate files. Table S1 shows sequences of PCR primers used in this study. Table S2 shows primary antibodies used in this study. Table S3 shows secondary antibodies used in this study. Table S4 shows sequences of siRNAs used in this study.